Title:
Distributed Radar Sounder: A Novel Concept for Subsurface Investigations Using Sensors in Formation Flight

This paper appears in:
IEEE Transactions on Geoscience and Remote Sensing

Date of Publication:
2019

Author(s):
Leonardo Carrer, Christopher Gerekos, Francesca Bovolo, Lorenzo Bruzzone

DOI:
10.1109/TGRS.2019.2929422

Distributed Radar Sounder: A Novel Concept for Subsurface Investigations Using Sensors in Formation Flight

Leonardo Carrer *Member, IEEE*, Christopher Gerekos, Francesca Bovolo *Senior Member, IEEE* and Lorenzo Bruzzone, *Fellow, IEEE*

***Abstract*—Spaceborne radar sounders are nadir-looking sensors operating in HF/VHF bands with subsurface sensing capabilities. Due to technological limitations, this type of sensors often deploy omnidirectional antennas. This results in undesired artifacts such as off-nadir clutter which could hinder data interpretation. Very recent technological advancements open up the possibility of synthesizing very large antenna apertures in HF/VHF band by using small satellites array deployed in suitable orbital formation flying. Accordingly, in this study we propose a novel concept of distributed radar sounder system. The proposed concept is complemented with a mathematical model for performance prediction which takes into account the uncertainty on the position of the sensors. Moreover, we discuss possible orbital solutions for the problem of the deployment of the distributed radar sounder system. The results show that a distributed radar sounder operating in small satellites formation flying is particularly appealing as it can (i) substantially reduce the impact of surface clutter, (ii) increase the across-track resolution, and (iii) increase the signal to noise ratio (or, alternatively, decrease the overall required transmitted power with respect to a traditional single configuration radar sounder design) and (iv) provide large flexibility in the data processing of the signals acquired by the different sensors.**

***Index Terms*—Radar Sounder, Radar, Formation Flight, Distributed System.**

I. Introduction

SPACEBORNE radar sounders are nadir-looking sensors mostly operating in the HF/VHF (*e.g.*, 1 MHz to 100 MHz) part of the electromagnetic spectrum. Such a low carrier frequency allows the transmitted electromagnetic waves to penetrate in the subsurface of a given terrain providing valuable information about its geophysical properties and structure.

These type of sensors have been deployed to sound the subsurface of planetary bodies such as Mars and the Moon [1][2], and are proposed for probing Jupiter's moons interior [3] and lava tubes concealed under the surface of the Moon [4]. In the context of Earth observation, a very interesting use of radar sounding is the study of the cryosphere and in particular the subsurface probing of the ice sheets of Antarctica and Greenland [5], [6] from space [7]. For this particular application, several international initiatives are taking place [7], [8], [9].

In the HF/VHF band, due to the long wavelength, technological limitations exist with respect to the type of the antenna deployable in space. For the past and the under development missions, the only type of antenna that has been adopted is a simple dipole mainly for mechanical reasons. The large antenna pattern of dipoles implies: (a) a very poor resolution in the across-track dimension with respect to the S/C movement, and (b) the presence of a significant across-track clutter that may hinder data interpretation. Moreover, for Earth observation applications a large antenna pattern will make the radar system more prone to unwanted radio frequency interference by human-generated radio sources. In the VHF band, there is the possibility of adopting different antenna solutions such as Yagi-Uda configuration [7] with respect to a dipole. This type of antenna would provide a higher gain with respect to the dipole solution but with a modest across-track beam selectivity (*i.e.*, limited clutter suppression capabilities). The challenges represented by the deployment strategy and antenna size persist also in this case. Thus the issues of effectively improve the across-track resolution and reduce the across-track clutter with alternative approaches remain open research problems for the radar sounding community.

Recent technological advancements open up the possibility of deploying a number of sensors in specific orbital formations flying for a number of microwave applications including imaging radars [10], [11], [12], [13]. Most of the work focuses on relatively higher frequency bands [14] (*i.e.*, UHF or higher) and different radar systems technologies (*e.g.*, side-looking SAR) than what addressed in this paper. The closest research field is related to distributed sensors array for low frequency radio astronomy from space operating in HF/VHF band [15][16] even though these are inherently passive systems.

The formation flying solution could overcome the current limitations on the antenna across-track beam-width imposed by the radar sounding relatively long wavelength. This can be achieved by synthesizing a very large across-track antenna aperture resulting from the sensors deployment configuration. The narrow beam in along-track direction is achieved through synthetic aperture processing. Accordingly, in this paper we explore a novel concept of spaceborne distributed radar sounding aimed at: (i) increasing the across-track resolution, (ii) reducing the clutter contribution and (iii) potentially increasing the signal to noise ratio by exploiting the simultaneous transmission of the different sensors. In Section II we propose a novel sensor deployment configuration and the related performance model for sizing and predicting the performance of the distributed radar sounder system. Section III is devoted to the theoretical modelling of the impact of uncertainties of the positions of the sensors on the sounding

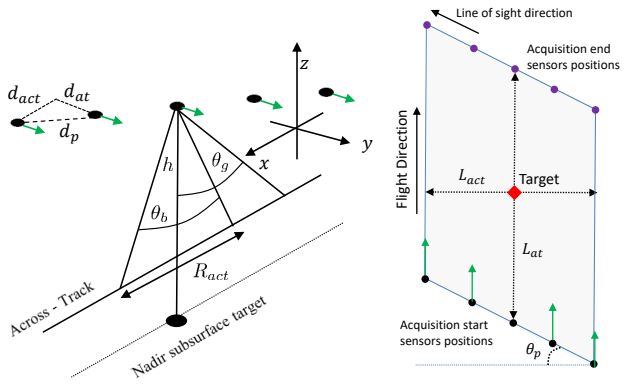

(a) (b)

Fig. 1: (a) Distributed Radar Sounder Geometry, green arrows indicate the sensors direction of movement (b) top-view illustration depicting how the equivalent antenna (grey area) is formed along with its shape. The value of θ_p is given by (1).

performances. Section IV discusses possible orbital solutions for the deployment of the designed distributed radar sounder system. Section V is devoted to the performance analysis of the envisioned distributed radar sounder. This is done by considering a meaningful application scenario where a comparison with an already proposed single configuration is possible. In Section VI a critical discussion on key technical implementation challenges is provided. Finally, Section VII provides the conclusions of this paper.

II. Geometry Configuration and Performance Mathematical Model

A. General System Design and Geometry Configuration

The main idea is to form a very large nadir-pointing antenna by exploiting the sensors formation flying in the across-track direction and synthetic aperture processing techniques based on sensors movement in the along-track one (Fig. 1 (a)). Moreover, we assume that each sensor is a point-like omnidirectional radiator and all the sensors transmit with the same initial phase.

Due to orbital deployment considerations (Section IV), we consider that the deployment axis of the sensors is not perpendicular to the along-track direction, but tilted from it by a rotation angle θ_p (Fig. 1 (b)).

Let N be the number of sensors forming the equivalent antenna and let d_{act} and d_{at} be their across-track and along-track mutual distances, respectively. The line of sight distance between each pair of sensors is equal to d_p. The rotation angle θ_p has the effect of rotating the synthesized antenna pattern in the along-track direction by an angular factor equal to (see Fig. 1 (b)):

$$\theta_p = \tan^{-1}\left(\frac{d_{at}}{d_{act}}\right) \tag{1}$$

According to Fig. 1 (b), the across-track equivalent antenna length L_{act} is equal to $(N-1)d_{act}$. In the along-track direction, the equivalent antenna length is given by unfocused synthetic aperture and thus equal to $L_{at} = \sqrt{\lambda h/2}$ [17], where h is the sensors altitude and λ the probing frequency wavelength.

The radar sounder resolution in the across-track and in the along-track directions denoted as R_{act} and R_{at} are equal to:

$$R_{act} = 0.886\ \theta_b\ h \tag{2}$$

$$R_{at} = \frac{\lambda h}{2L_{at}} = \sqrt{\lambda h/2} \tag{3}$$

The across-track equivalent antenna beam-width denoted as θ_b is given by:

$$\theta_b = \frac{\lambda}{L_{act}} = \frac{\lambda}{(N-1)d_{act}} \tag{4}$$

The radar sensor array can be sized by defining the value of θ_b to obtain the desired resolution. Unfortunately, θ_b cannot be arbitrary small under the assumption that all sensors are emitting with the same initial phase. We assume that the relative position of the sensors is such that the distributed radar always forms a coherent aperture. Accordingly, the following condition on radiation coherence within the across-track synthesized antenna aperture must be satisfied:

$$\sqrt{\left(\frac{L_{act}}{2}\right)^2 + h^2} - h \leqslant \frac{\lambda}{4} \tag{5}$$

The substitution of (4) into (5) results in the following inequality:

$$\theta_b \geq \sqrt{\frac{\lambda}{2h}} \tag{6}$$

By substituting the result of (6) in (2), the best achievable across-track resolution is equal to $R_{act} = 0.886\sqrt{\lambda h/2}$ which is approximately equal to the first Fresnel zone. The sensors formation synthesize an across-track antenna pattern with the first grating lobe (*i.e.*, peak ambiguity) defined as θ_g at an angular position described by [18]:

$$\sin(\theta_g) = \lambda/d_{act} \tag{7}$$

The values of θ_g and θ_b shall be a-priori selected according to the application needs. The value of the grating lobe can be constrained according to the maximum expected penetration depth z_p and expected subsurface dielectric constant ϵ_r as follows (see Fig. 2):

$$\theta_g \geq \cos^{-1}\left(\frac{h}{h + \sqrt{\epsilon_r} z_p}\right) \tag{8}$$

Equation (8) defines the maximum off-nadir angle, which corresponds to θ_g, at which clutter contributions can be expected. In real applications a margin shall be taken with respect to the value provided by (8).

By combining (4) and (7) we can compute N specifying the number of sensors such that the first ambiguity will be at θ_g satisfying the resolution constrain dictated by θ_b as follows:

$$N = \left\lceil \frac{\sin(\theta_g)}{\theta_b} \right\rceil + 1 \tag{9}$$

We assume that N is odd, so that a central element exists, with an equal number of elements on either side. Finally, the

sensors distance d_{act} is computed by inverting (4) and by using the value of N derived from (9):

$$d_{act} = \frac{\lambda}{(N-1)\theta_b} \tag{10}$$

Under the assumption of coherent aperture, the maximum value of d_{at} is derived as:

$$d_{at} \leq \sqrt{d_p^2 - d_{act}^2} \tag{11}$$

The line of sight distance between sensors d_p is bounded to:

$$d_p \leq \frac{\sqrt{2\lambda h}}{N-1} \tag{12}$$

The result of (12) is equivalent to state that the antenna length in the line of sight direction should be equal to the first fresnel diameter (coherence condition).

The value of θ_p resulting from (1) depends on d_{at} and may be such that the secondary diffraction peak given by the grating lobe of (8) folds inside the sounding scene. The dimension of the useful sounding scene is dictated by the maximum penetration depth z_p and it is equal to a circle with equivalent radius d_1 defined as (see Fig. 3):

$$d_1 = [(h + z_p\sqrt{\epsilon_r})^2 - h^2]^{1/2} = [2hz_p\sqrt{\epsilon_r} + z_p^2\epsilon_r]^{1/2} \tag{13}$$

The maximum value of θ_p denoted as $\theta_{p,max}$ and, in turns, of d_{at} for no peak ambiguities folded within the scene is derived as follows from geometric considerations (see Fig. 3):

$$\theta_{p,max} = \tan^{-1}\sqrt{\left(\frac{d_2}{d_1}\right)^2 - 1} \tag{14}$$

where the equivalent ground position of the peak ambiguity d_2 is defined as:

$$d_2 = h\tan(\theta_g) \tag{15}$$

It follows from (8) that $d_2 \geq d_1$. Therefore the maximum allowable value of d_{at} is equal to the minimum between the value provided by the coherence condition of (11) and the no ambiguity condition within the scene of (14):

$$d_{at} = \min\left\{d_{act}\tan\theta_{p,max}, \sqrt{d_p^2 - d_{act}^2}\right\} \tag{16}$$

The described equations define the geometric configuration of the distributed sounder system to meet certain requirements. In the next section we evaluate the actual improvement in signal to noise ratio and resolution as a function of the parameters with respect to the standard radar sounder case.

B. Resolution and SNR Improvement

In a radar sounder the across-track resolution is commonly assumed to be equal to the pulse-limited diameter [17], denoted as D_{pl}, which is equal to:

$$D_{pl} = 2\sqrt{\frac{c_0 h}{B}} \tag{17}$$

where B is the transmitted bandwidth and c_0 the speed of the light in vacuum.

If $1/B$ exceeds the pulse width T_s then we refer to the time-limited diameter D_{tl} which is equal to:

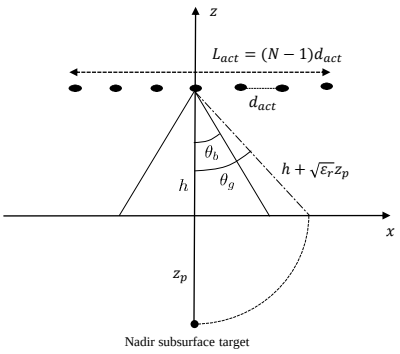

Fig. 2: Across-track section view.

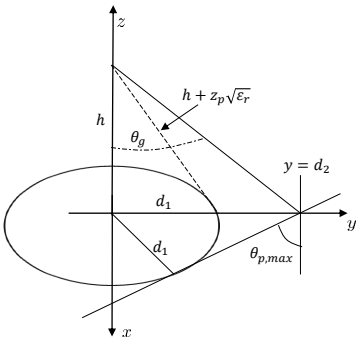

Fig. 3: Geometry sketch for $\theta_{p,max}$ definition.

$$D_{tl} = 2\sqrt{c_0 h T_s} \tag{18}$$

We define the across-track resolution improvement factor $IRF(\theta_b)$ of the distributed sounding radar with respect to a single sounding configuration as:

$$IRF(\theta_b) = \frac{D_{pl}}{R_{act}} = \frac{2}{0.886\theta_b}\sqrt{\frac{c_0}{Bh}} \tag{19}$$

A notable case of the above expression is when the across-track equivalent beam-width is equal to the lower bound of (6) resulting in:

$$IRF\left(\theta_b = \sqrt{\frac{\lambda}{2h}}\right) = \frac{2\sqrt{2}}{0.886}\sqrt{\frac{c_0}{B\lambda}} \tag{20}$$

This implies that the distributed sounder across-track resolution improvement factor mainly depends on the inverse of the fractional bandwidth of the radar system. The minimum value of IRF occurs when $\sqrt{c_0/B\lambda} = 1/\sqrt{2}$ (this corresponds to 100% relative fractional bandwidth). The maximum occurs when B tends to 0. In this particular case, D_{pl} in (19) should be replaced with D_{tl} in (18) as the pulse width T_s is smaller than $1/B$. Therefore the value of IRF is bounded by:

$$\frac{2}{0.886} \leq IRF \leq \frac{2\sqrt{2}}{0.886}\sqrt{\frac{c_0 h T_s}{\lambda}} \tag{21}$$

It is important to note that the condition $1/B > T_s$ is unlikely to occur in real radar sounding applications since very often a linear frequency modulation of the transmitted pulse is used.

In radar sounding, SNR plays an important role in determining the maximum penetration depth of the system which

is one of the main performance factors for this type of system. To this extent, let us consider the overall received power P_r by the distributed radar sounder from the surface:

$$P_r = \frac{N_t^2 N_r^2 N_{at}^2 P_t G_0^2 \sigma \lambda^2}{(4\pi)^3 h^4} \tag{22}$$

where σ is the radar cross section of a given target, G_0 and P_t are the gain and transmitted power (assumed equal for each individual sensor) respectively, N_r and N_t are the total number of receiving and transmitting sensors respectively. The number of pulses recollected for each target by the synthetic aperture is denoted as $N_{at} = \lfloor L_{at}/(v_s \cdot PRI) \rfloor$ where the distance between elements is computed as $v_s PRI$ and v_s is the sensors velocity and PRI the pulse repetition interval. N_{at} corresponds to the equivalent number of sensors deployed in the along-track direction. We assume without loss of generality that the acquisition is centred over the target, leading to the condition that N_{at} is odd. The interested reader can refer to Appendix A for the main assumptions and derivation of (22).

The noise power P_b is equal to [19]:

$$P_b = N_r^2 N_{at} \cdot k_b T B \tag{23}$$

where k_b and T are the Boltzmann's constant and the galactic or human-made source equivalent noise temperature. T and B are assumed to be equal for all the array sensors. The noise power behaves as N_r^2 under the assumption that the external noise source is correlated among receivers for each fixed along-track position but uncorrelated as the sensors move along the orbit. If the noise source is not correlated among receivers, then a factor equal to N_r should be assumed in (23) instead of N_r^2.

The surface signal to noise ratio (SNR) is equal to:

$$SNR = \frac{P_r}{P_b} G_r = \frac{N_t^2 N_{at} P_t G_0^2 \sigma \lambda^2}{(4\pi)^3 h^4 k_b T B} G_r \tag{24}$$

The range compression gain is defined as $G_r = B \cdot T_s$.

A single sensor performing a synthetic aperture is equivalent to assume $N_t = N_r = 1$. By considering the most simple case of sensor array configuration such that $N_r = N_t = N$, the distributed sensor array has a SNR improvement with respect to a single radar equal to N^2. This is derived by assuming that (i) all the deployed sensors transmit and receive simultaneously and (ii) the value of d_{at} is selected according to (16). If the external noise sources are spatially uncorrelated then there is an additional SNR gain equal to N_r. Therefore the SNR gain for this particular configuration can range from N^2 (worst case) to N^3 (best case).

Another possible sensor configuration is to have one central transmitting element (i.e, mother ship) and all the other deployed sensors receiving. In this case, the SNR of (24) is reduced by a factor N_t^2 and the resolution in across-track worsen by a factor of $\sqrt{2}$ with respect to the configuration with all elements transmitting and receiving simultaneously.

In the case that d_{at} exceeds the bound of (16), it is possible to perform a sequential acquisition strategy such that each element transmits and receives separately. In this case, the SNR of (24) is reduced by a factor N_r (only in the case of spatially uncorrelated noise sources) and the resolution in across-track improves by a factor of $\sqrt{2}$ with respect to the configuration where all elements are transmitting and receiving simultaneously. This is due to the fact that the array pattern is effectively synthesized at an equivalent distance of $2h$ rather than h (see (6)).

In general, the distributed sounder two-way antenna gain is equal to $N_t^2 G_0^2$. This implies that the entire gain N_t^2 or an integer fraction of it can be actually used to distribute the total overall required power P_t over N_t sensors (*i.e.*, each sensor transmits P_t/N_t^2). On the one hand, this is a particularly interesting feature for sounding applications where a large amount of power is required but may not be technological feasible to transmit on a single transmitter. On the other hand, increasing the Tx power for all sensors has implications on the complexity of the related platform.

C. Radiation Intensity

In this section, we provide the mathematical model for computing the ground radiated intensity distribution with respect to the time-varying sensors positions. We assume that the sensor array is deployed along the x axis and the unfocused synthetic aperture is performed along the y axis (see Fig. 1). Under the assumption of an odd number of sensors, the varying position of the sensor in the across-track direction is equal to $x_{nm} = n d_{act}$, with

$$n = -(N-1)/2, ..., (N-1)/2, \tag{25}$$

so that the central element of the array lies at the origin of the axis. The index n both represents the sensor element number and its spatial position in across and along track when its multiplied by d_{act} or d_{at} respectively. In the along-track direction, the position of the sensors is defined by $y_{nm} = n d_{at} + m\Delta y$, where

$$m = -(N_{at}-1)/2, ..., (N_{at}-1)/2, \tag{26}$$

and $\Delta_y = v_s \cdot PRI$.

The euclidean distance between any given sensor nm at a position $\mathbf{p}_{nm} = (x_{nm}, y_{nm}, h\mathbf{1}_{nm})$ and a flat surface of unspecified dimensions laying in the x-y plane is equal to:

$$d_{nm}(x,y) = \sqrt{(x - x_{nm})^2 + (y - y_{nm})^2 + h^2}. \tag{27}$$

Assuming every array element emits an harmonic field with identical initial phase, the total electric field at any given point (x, y) of the surface is given by :

$$\begin{aligned} \Psi(x,y) &= \sum_n \sum_m \frac{A_{nm}}{d_{nm}(x,y)} e^{jk d_{nm}(x,y)}, \\ &\equiv \sum_n \sum_m \psi_{nm}(x,y), \end{aligned} \tag{28}$$

where n and m take the values given in eqs. (25) and (26), respectively, A_{nm} the amplitude of the field emitted by array element (n, m), and k the wave number of the harmonic field. The one-way radiation intensity $U(x, y)$ is given by:

$$U(x,y) = \Psi(x,y)\Psi^\dagger(x,y), \tag{29}$$

where the dagger symbol represent represents the Hermitian conjugate.

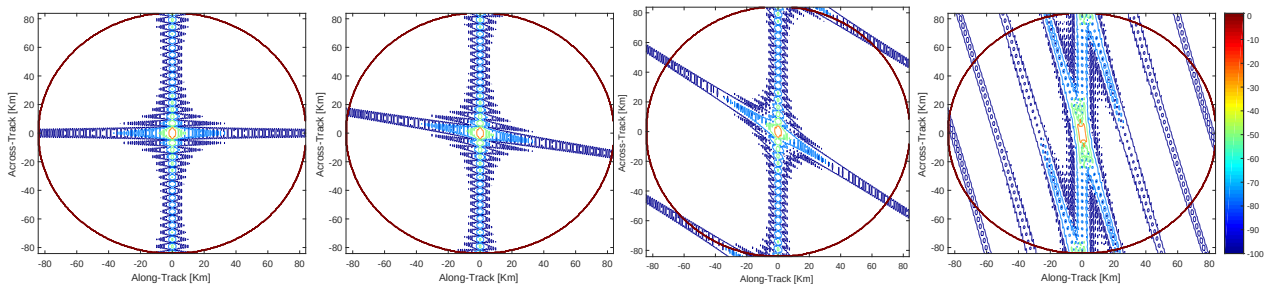

(a) (b) (c) (d)

Fig. 4: Normalized two-way radiation intensity $\hat{U}^2(x,y)$ contour plots in dB for (a) $\theta_p = 0$, (b) $\theta_p = 10^\circ$, (c) $\theta_p = 33^\circ$ and (d) $\theta_p = 74^\circ$. The plots are relative to the all sensors simultaneously transmitting and receiving configuration. The last case corresponds to the maximum allowable value of d_{at} (see (11)) while the case displayed in Figure (c) corresponds to $\theta_{p,max}$ (see (14)). Red circles correspond to the maximum equivalent surface radius for which subsurface returns are expected (see (13)). $\hat{U}(x,y)$ has been computed assuming $\lambda = 6.66$ m, $h = 500$ Km, $N = 21$, $z_p = 4$ Km, $\theta_g = 11.5^\circ$, $\epsilon_r = 3.1$ and $\theta_b = 0.59^\circ$.

Fig. 4 shows different examples of contour plots of the two-way normalised radiation intensity $\hat{U}^2(x,y)$ of (29) as function of θ_p (see (1)).

The reference one-way radiation intensity U_0 obtained considering a single point-like radiator (i.e. single configuration radar sounder) positioned in $(x,y,z) = (0,0,h)$ only performing along-track focusing can be computed assuming $N = 1$ in the previous equations, which removes the sum over n :

$$U_0(x,y) = \Psi_0(x,y)\Psi_0^\dagger(x,y) \tag{30}$$

where

$$\Psi_0(x,y) = \sum_m \frac{A_m}{d_m(x,y)} e^{jkd_m(x,y)}, \tag{31}$$

$$d_m(x,y) = \sqrt{x^2 + (y - m\Delta y)^2 + h^2}. \tag{32}$$

D. Clutter Improvement Factor

For the evaluation of the clutter improvement factor, we assume that the clutter returns for a given penetration depth δ will arise from an annulus. The annulus area depends on the projection of the range resolution R_r on ground and on the off-nadir angle θ. Accordingly, the clutter improvement factor $C_g(\delta)$ as function of the penetration depth δ is defined as:

$$C_g(\delta) = \frac{\int_{-\pi}^{\pi}\int_{\rho_1}^{\rho_2} \hat{U}_o^2(\phi,\rho)\ \rho d\rho d\phi}{\int_{-\pi}^{\pi}\int_{\rho_1}^{\rho_2} \hat{U}^2(\phi,\rho)\ \rho d\rho d\phi} \tag{33}$$

where $\hat{U}$ and $\hat{U}_0$ are the normalised versions of the intensities U and U_0 given above. The coordinate transformation from Cartesian to polar reference frame are $\rho = \sqrt{x^2+y^2}$ and $\phi = \arctan(y/x)$. The radial integration $\rho_1 = h\tan\theta - R_r/(2\sin\theta)$ and $\rho_2 = h\tan\theta + R_r/(2\sin\theta)$. The off-nadir angle $\theta = \arccos(h/(h+\delta))$.

$C_g(\delta)$ is a metric that considers the ratio of two antenna patterns. Therefore it may display a rippling behaviour. Accordingly, to quantify the capability of clutter suppression of a given synthesised array, we will assume as performance metric the maximum value of the lower envelope of $C_g(\delta)$ (see Fig. 5).

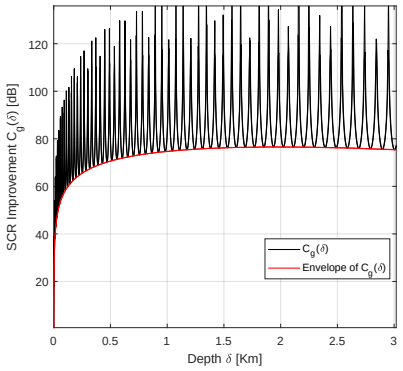

Fig. 5: Example of behaviour of the signal to clutter improvement $C_g(\delta)$ as a function of the penetration depth δ. The figure has been computed considering $\lambda = 6.66$ m, $N = 92$, $\theta_g = 13.44^\circ$, $h = 500$ Km.

III. Impact of Sensors Spatial Position Uncertainty

In Section II-C, the two-way radiation pattern for an ideal distributed radar sounder has been derived. In this Section, we first characterise this pattern in presence of uncertainties in the positions of the deployed sensors. Based on that, we derive performance metrics for evaluating the distributed radar peak power loss and peak to side lobe ratio resulting from inaccuracies in the position of the sensors.

To evaluate the impact of such uncertainties on the shape of the radiation intensity $U(x,y)$ (see (29)), we add a Gaussian perturbation to the position of the distributed sounder elements and we derive the expression for the ensemble-averaged perturbed pattern using stochastic analysis. In particular, we derive the average perturbed pattern and its simplified formulas for nadir and off-nadir regime. Then, by analysing the properties of the average perturbed pattern, performance metrics are derived.

As the along-track dimension of the array is obtained by synthetic aperture techniques (see Fig. 1), we assume that the along-track perturbations are inherited from the ones of each sensor at the beginning of the acquisition. Consequently, we

take advantage of the translational symmetry of the problem in the y-direction and evaluate perturbations on a *linear* array. This is equivalent of setting $N_{at} = 1$ in (28), which removes the sum over m. Thus we assume without loss of generality that $y = 0$. This is equivalent to defining a system of coordinates aligned with the line of sight axis of the array (see Fig. 1 (b)). Therefore, for the following analyses, we assume an inter-element distance equal to d_p and a line of sight antenna length L given by $L = L_{act}/\cos\theta_p$. Moreover we assume for simplicity that all array elements radiate with an identical amplitude $A_n = A$, $\forall n$.

We start by introducing a perturbation in the position $\mathbf{p}_n$ of each element of the array, which has the form of a random vector $\boldsymbol{\delta}_n = (\delta_n^x, \delta_n^y, \delta_n^z)$:

$$\mathbf{p}_n \to \mathbf{p}_n + \boldsymbol{\delta}_n = (x_n + \delta_n^x, \delta_n^y, h + \delta_n^z) \tag{34}$$

We assume that those perturbations are all drawn from independent, zero-mean Gaussian distributions: $\delta_n^x \sim \mathcal{N}(\mu = 0, \sigma_x)$, $\delta_n^y \sim \mathcal{N}(\mu = 0, \sigma_y)$ and $\delta_n^x \sim \mathcal{N}(\mu = 0, \sigma_z)$ where σ_x, σ_y, and σ_z are the standard deviations characterising the perturbations in the x-, y-, and z-directions, respectively. The perturbed electric field $\tilde{\Psi}$ is obtained by inserting the perturbed satellite positions of (34) in (28). Then the average perturbed radiation intensity $\langle \tilde{U}(x,y) \rangle$ is computed as the ensemble-average of the squared norm of the perturbed electric field $\tilde{\Psi}$ over the δ_x, δ_y, and δ_z [1]:

$$\left\langle \tilde{U}(x,y) \right\rangle_{\delta_x,\delta_y,\delta_z} = \left\langle \tilde{\Psi}(x,y)\tilde{\Psi}^\dagger(x,y) \right\rangle_{\delta_x,\delta_y,\delta_z}. \tag{35}$$

Appendix B shows that the above expression is equal to:

$$\left\langle \tilde{U}(x,y) \right\rangle_{\delta_x,\delta_y,\delta_z} = \sum_n |\psi_n|^2 + \sum_n \sum_{n'} \left[I - \delta_{nn'}\right] \psi_n {\psi'_n}^\dagger \, e^{-\frac{1}{2}k^2\left[\left[(\Delta_n^x)^2 + (\Delta_{n'}^x)^2\right]\sigma_x^2 + \left[(\Delta_n^y)^2 + (\Delta_{n'}^y)^2\right]\sigma_y^2 + \left(\frac{h^2}{d_n^2} + \frac{h^2}{d_{n'}^2}\right)\sigma_z^2\right]}, \tag{36}$$

where $\Delta_n^x \equiv \frac{x - x_n}{d_n}$ and $\Delta_n^y \equiv \frac{y}{d_n}$ are the x- and y-direction relative distances between the array element n and the flat surface.

Fig. 6 displays the two-dimensional average perturbed patterns obtained through (36) for several values of σ_x, σ_y and σ_z along with the unperturbed pattern. The behaviour of $\langle \tilde{U}(x,y) \rangle_{\delta_x,\delta_y,\delta_z}$ shows several interesting features: (i) The peak width remains constant for any perturbation, regardless of direction and amplitude, (ii) x and y-direction perturbations have almost no effect on the peak height, they only affect far off-nadir regions, (iii) z-direction perturbations strongly affect the peak height, and seem to show an easily predictable background level, and (iv) y-direction perturbations limit the antenna pattern in the along-track direction.

The main consequence of perturbations being frozen in the along-track direction is that the radiation pattern of the complete array (physical and with synthetic aperture processing) is simply given by the perturbed pattern of the physical array superimposed on an along-track cardinal sinus function, whose width is determined by the synthetic aperture length. Fig. 7 displays the patterns of an array for a single realization of the perturbation of Fig. 6 (g), with and without SAR processing, and with a rotation angle $\theta_p = 30°$. Fig. 7 (a) shows that a single realization of the perturbation matches the results of the ensemble-averaged formula (Fig. 6 (g)), whereas the comparison of Fig. 7 (a) and (b) illustrates the property we have just mentioned. This confirms that the perturbation analysis of the physical array only, which allows derivation of reduced formulas, is sufficient for understanding the effect of perturbations regardless of whether synthetic aperture processing is applied.

[1]We will drop the n indices on the perturbations when the context is sufficiently clear.

A. Reduced formula

While (36) captures the full perturbative behaviour of the radiation pattern, it contains unreduced sums. In the following, we derive a closed-form of expression (36) by making additional assumptions: (i) The patterns observed correspond to those of uni-dimensional diffraction grating, affected by distortions due to non-paraxiality of the setting and to the planar projection surface. These cases can be treated using optical theory of aberrations [20]. However, in practice, the sounder array will always be designed such that the first grating lobe is far from the echo generated by the deepest feature of interest (as in Section V). The consequence of this design choice is that, for the region of interest, the paraxial approximation is very good. (ii) The x-direction perturbations are not significantly smaller than the y-direction perturbations. This assumption is reasonable from an engineering point of view, and allows us to greatly simplify the problem of deriving reduced quantities. Indeed, in this case, the ensemble-averaged perturbed pattern is identical to a very high degree of approximation for all directions except the pure y-direction.. For a tilted array, the direct consequence of this assumption is that the nadir and background patterns in the along-track and across-track direction and as well as in the direction of the axis of the antenna are practically the same.

Given these two assumptions, paraxiality and $\mathcal{O}(\sigma_x) = \mathcal{O}(\sigma_y)$, we may focus our analysis on the changes in power in the x-direction. We will use the cartesian coordinate x or the off-nadir angle in the direction parallel to the axis of the antenna $\theta = \tan(x/h)$ interchangeably.

We assume we can factorise the perturbed-averaged pattern as follows:

$$\left\langle \tilde{U}(\theta) \right\rangle = P_{\text{incoh}}(\theta) + e^{-f(\sigma_x,\sigma_y,\sigma_z)}\left[P_{\text{coh}}(\theta) - P_{\text{incoh}}(\theta)\right], \tag{37}$$

(the δ_x, δ_y, δ_z subscripts specifying the process over which the ensemble-averaging operation is carried out has been dropped for clarity). $P_{\text{incoh}} = \sum_{n=1}^{N} |\psi_n|^2$ is the isotropic, incoherent component arising from the stochastic character of the position errors, P_{coh} represents the unperturbed component (which is naturally fully-coherent), and $f(\sigma_x, \sigma_y, \sigma_z)$ is an *a priori* unknown function, which will be determined in the next paragraphs by exploiting (36). If f is large, the coherent component of the power vanishes, leaving only the incoherent background power. On the other hand, when f is very small only the coherent component subsists.

The incoherent component is straightforward to compute, and, in the paraxial region, the coherent component is the

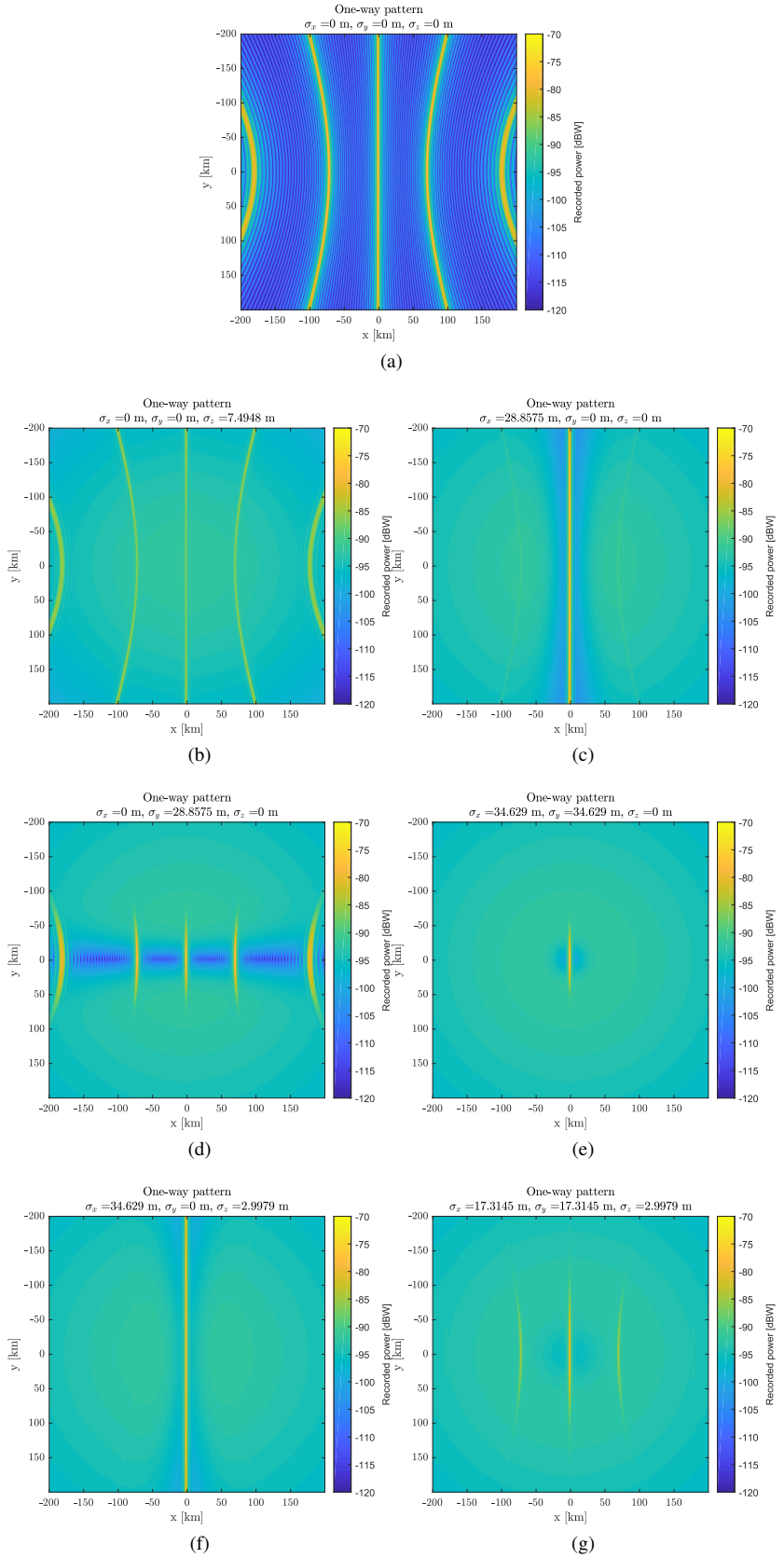

(a) (b) (c) (d) (e) (f) (g)

Fig. 6: Comparisons between unperturbed and average perturbed patterns for an array characterized by $f = 10$ MHz, $\lambda = 30$ m, $h = 200$ km, $L = 80\lambda$, $d_{act} = 3\lambda$, $N = 27$. (a) Unperturbed pattern. (b) $\sigma_z = \lambda/4$. (c) $\sigma_x = R_{1F}/60$ (d) $\sigma_y = R_{1F}/60$. (e) $\sigma_x = R_{1F}/50$, $\sigma_y = R_{1F}/50$. (f) $\sigma_x = R_{1F}/50$, $\sigma_z = \lambda/10$. (g) $\sigma_x = R_{1F}/100$, $\sigma_y = R_{1F}/100$, $\sigma_z = \lambda/10$. The variable denoted as $R_{1F} = \sqrt{\lambda h/2}$ is the first Fresnel radius.

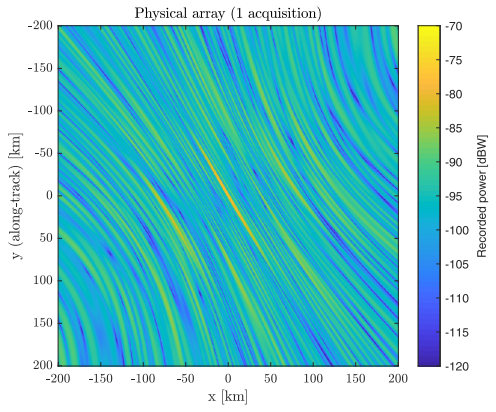

(a)

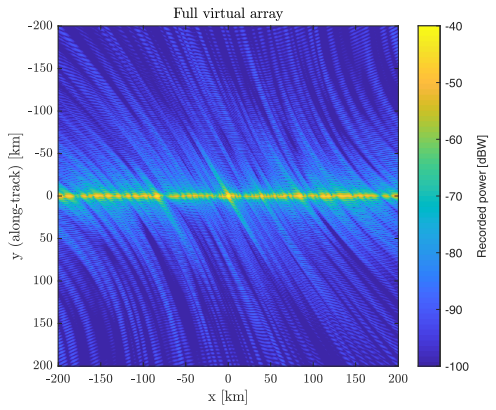

(b)

Fig. 7: Illustration of the effect of SAR focusing on the perturbed pattern, shown on a single realization of the perturbation of Fig. 6 (g). (a) Pattern of a physical array. (b) Pattern of the same array with unfocused SAR processing ($L_{at} = R_{1F}$, $d_{at} = 20$ m). The considered array is the same as that in Fig. 6, with a rotation angle $\theta_p = 30°$.

pattern generated by a collection of equidistant point emitters distributed over a finite length, which is well-known (e.g., [21]). We obtain:

$$P_{\text{incoh}}(\theta) = A^2 \frac{N}{h^2} \cos^2\theta, \tag{38}$$

$$P_{\text{coh}}(\theta) = \frac{A^2}{h^2} \frac{\sin^2\left(\frac{Nd_p}{\lambda}\pi \sin\theta\right)}{\sin^2\left(\frac{d_p}{\lambda}\pi \sin\theta\right)}. \tag{39}$$

To determine $f(\sigma_x, \sigma_y, \sigma_z)$, we first assume that, in *real* exponentials, the distance between any array element and any point is given by the platform altitude: $d_n(x, y) = h \ \forall n$. Additionally, we need to define an order of magnitude for the Δ_n^x and Δ_n^y factors that appear in the exponential. Due to the peculiar form of expression (36), we model nadir regions and off-nadir regions in a different way.

1) Nadir case: At nadir, the unperturbed coherent power of (39) reduces to $P_{\text{coh}}(0) \approx A^2 \frac{N^2}{h^2}$, as all waves reach that point almost perfectly in phase.

A reasonable value for $x - x_n$ is $L/4$, the midpoint between the array centre and the tip of the array. In the y-direction, $y - y_n = 0$ since $y = 0$ and $y_n = 0 \ \forall n$ as we assume that the physical array is deployed in the x-direction. Thus, we have $(\Delta_n^x)^2|_{(x,y)=(0,0)} \approx (L/4h)^2$ and $(\Delta_n^y)^2|_{(x,y)=(0,0)} = 0$. By applying the above observations to (36) and by considering (37), in the nadir case the perturbed-averaged pattern of (37) is equal to:

$$\left\langle \tilde{U}(\theta) \right\rangle^{\text{nad}} \equiv \left\langle \tilde{U}(\theta \approx 0) \right\rangle \approx A^2 \frac{N}{h^2} \left[\cos^2\theta + e^{-k^2\left[\left(\frac{L}{4h}\right)^2 \sigma_x^2 + \sigma_z^2\right]} (N - \cos^2\theta) \right] \tag{40}$$

From (40), we can observe that the $e^{-k^2\sigma_z^2}$ dependence of the second term of expression makes the peak height very sensitive to z-direction errors, but not for x-direction perturbations. Indeed, for typical array configuration, we have $L = \mathcal{O}(10^2 m)$ and $h = \mathcal{O}(10^5 m)$, which makes $\left(\frac{L}{4h}\right)^2 = \mathcal{O}(10^{-6})$. This explains why x-perturbations show no effect on the peak height in the two examples shown in Fig. 6. Indeed σ_x needs to be very large to counteract its small prefactor and affect peak height.

2) Off-nadir case: To derive the closed form expression of (37) for the background power, we consider that $x - x_n \approx y - y_n \approx h/2$. In principle, this is only valid when the off-nadir angle is equal to $\pi/8$. However, in practice, the difference across all points which cannot be considered at nadir is never higher than few dB for typical orbital radar sounder scenarios. With those approximations we obtain $(\Delta_n^x)^2|_{(x,y)\approx(h/2,h/2)} \approx (\Delta_n^y)^2|_{(x,y)\approx(h/2,h/2)} \approx 1/4$.

Therefore, (37) reduces to the following expression for "large" off-nadir angles ($\theta \gg 0$):

$$\left\langle \tilde{U}(\theta) \right\rangle^{\text{bg}} \equiv \left\langle \tilde{U}(\theta \gg 0) \right\rangle \approx A^2 \frac{N}{h^2} \left[\cos^2(\theta) + e^{-\frac{k^2}{4}\left(\sigma_x^2 + \sigma_y^2 + 4\sigma_z^2\right)} \left(\frac{1}{N} \frac{\sin^2\left(\frac{Nd_p}{\lambda}\pi \sin\theta\right)}{\sin^2\left(\frac{d_p}{\lambda}\pi \sin\theta\right)} - \cos^2\theta \right) \right] \tag{41}$$

One can see that, away from nadir, perturbations in the x- and y- directions have an effect of comparable magnitude to z-direction perturbations, supporting the preliminary analysis of $\langle \tilde{U} \rangle$ in Fig. 6.

Fig. 8 compares the average perturbed pattern $\langle \tilde{U} \rangle$ along with its two simplifications $\langle \tilde{U} \rangle^{\text{nad}}$ and $\langle \tilde{U} \rangle^{\text{bg}}$. One can observe that $\langle \tilde{U} \rangle^{\text{nad}}$ matches $\langle \tilde{U} \rangle$ for small angles, whereas $\langle \tilde{U} \rangle^{\text{bg}}$ matches it for large angles, as expected (the unperturbed pattern U is also plotted for reference).

B. Performance degradation metrics

The distributed radar sounder performance degradation in terms of power loss and side lobes degradation due to positioning inaccuracy can be described in terms of (i) the peak power loss at nadir and, (ii) the peak-to-background ratio.

The one-way peak power loss at nadir $P_{L,\text{nadir}}$ is defined as:

$$P_{L,\text{nadir}} = \frac{\langle \tilde{U}(0) \rangle^{\text{nad}}}{P_{\text{coh}}(0)} = \frac{1}{N} + e^{-k^2\left[\left(\frac{L}{4h}\right)^2 \sigma_x^2 + \sigma_z^2\right]} \left(1 - \frac{1}{N}\right) \tag{42}$$

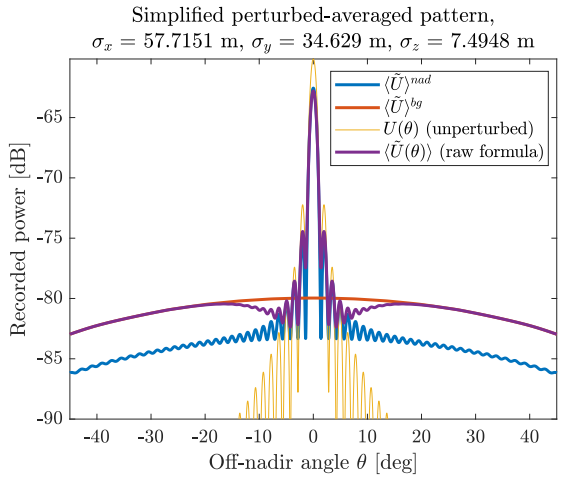

Fig. 8: Comparison between the simplified pattern for nadir $\langle\tilde{U}\rangle^{\text{nad}}$ (blue curve) and that for off-nadir zones $\langle\tilde{U}\rangle^{\text{bg}}$ (orange curve) from (40) and (41) against the actual perturbed-averaged pattern $\langle\tilde{U}\rangle$ (purple curve) from (36). An array with the following characteristics is considered : $f = 5$ MHz, $\lambda = 60$ m, $h = 100$ km, $L = 40\lambda$, $d_{act} = 0.4\lambda$, $N = 101$. For reference, the unperturbed pattern U from (29) is shown in yellow.

The average perturbed peak-to-background ratio losses, $P_{L,\text{bg}}$, measured at a given off-nadir angle $\hat{\theta}$ is given by:

$$P_{L,\text{bg}}(\hat{\theta}) = \frac{\langle\tilde{U}(\hat{\theta})\rangle^{\text{bg}}}{\langle\tilde{U}(0)\rangle^{\text{nad}}} \frac{P_{\text{coh}}(0)}{P_{\text{coh}}(\hat{\theta})} \tag{43}$$

As first approximation for evaluating performance, the angle $\hat{\theta}$ can be selected as $\hat{\theta} \approx \theta_g/2$. The two-way losses can be easily computed as $P^2_{L,\text{nadir}}$ and $P^2_{L,\text{bg}}$.

In terms of radar sounder system performance, the peak power loss (42) impacts the penetration capabilities of the instrument, whereas the peak to back ground ratio (43) affects the clutter suppression capabilities of the instrument.

IV. Orbit Design

In this section, possible solutions for the orbital configuration of the distributed radar sounder are discussed. Section IV-A proposes acceptable orbit configurations based on Keplerian mechanics whereas Section IV-B discusses orbital perturbations. Orbital perturbation equations are only valid for a non-spherical body where the J_2 coefficient of its gravitational potential is much larger than any other multipole (such as for Earth) [22].

A. Analysis of Possible Orbit Configurations

Without loss of generality, we consider a working configuration deployed in polar orbit where the required equivalent across-track antenna length L_{act} (see Section II-A) is achieved by varying the inclination of the orbits of each array element n by increments with respect to the central one positioned at an inclination of $i_0 = 90°$. The eccentricity denoted as e_n is set to zero for all the sensors, making the argument of perigee ω_n undefined. The inclination increment is given by the ratio of the across-track sensors spacing d_{act} to the distance from the center of gravity of Earth, $R_\oplus + h$. The inclination i_n of a given array element n is thus given by:

$$i_n = \frac{\pi}{2} + n \arctan \frac{d_{act}}{R_\oplus + h} \tag{44}$$

This configuration provides the required across-track equivalent antenna length $L_{act} = (N-1)d_{act}$ over the poles and a zero baseline over equatorial regions, where orbits intersect (Fig. 9-a). To avoid the satellites from colliding with each other at the intersection points, the true anomalies ψ_n of the satellites must also be individually tweaked (see Fig. 9-b). While any function $f_n(d_{at})$ (where d_{at} is the along-track safety distance) would be suitable, we considered throughout this paper arrays with a linear evolution of the along-track increments for simplicity. Consequently, the true anomalies of each array element are defined incrementally as follows:

$$\psi_n = n \arctan[d_{at}/(R_\oplus + h)] \tag{45}$$

where d_{at} is smaller than or to than the bound of (16).

The above observations implicitly assume a zero right ascension of the ascending node (RAAN) for each sensor ($\Omega_n = 0, \forall n$). However, by varying Ω_n, it is possible to move the latitude of the intersection points of the orbits, allowing the configuration to achieve the required L_{act} at almost any target latitude (Fig. 9-c). Let the intersection point be located at a positive x coordinate (the other one is simply shifted by $180°$ along the orbit), and denote it with r^*. The locus of points that are common to a reference polar orbit with $i_0 = 90°, \Omega_0 = 0$ and to an orbit with arbitrary i and Ω can be determined by solving a simple system of equations. The colatitude of this intersection point is given by: [2]

$$r^*_\phi = \arctan\left[2\,\text{sgn}(\Omega)\frac{1-\sqrt{\sec\Omega - 1}\cos i - \sec\Omega}{\cos i\left(\cos i + 2\sqrt{\sec\Omega - 1}\right)}\right]. \tag{46}$$

The value Ω_n for a crossing point at a given r^*_ϕ can be obtained by numerically inverting (46) for Ω. We name this inverse function g, so that $\Omega_n = g(i_n, r^*_\phi)$.

In the next section, we evaluate the orbital perturbations of the sensors induced by nodal and apsidal precession.

B. Orbital perturbations

The nodal precession rate (denoted as $\Delta\Omega$) proceeds is given by:

$$\Delta\Omega_n = -\frac{3\pi J_2 R^2_\oplus}{(R_\oplus + h)^2(1-e_n^2)^2}\cos i_n \quad \text{rad/orbit}, \tag{47}$$

where J_2 is the second dynamic form factor of the considered celestial body. In the Earth case, $J_2 \approx 1.082 \times 10^{-3}$ [22]. The central array element ($i_0 = 90°$) experiences no nodal precession. We can assume that $d_{act} \ll h + R_\oplus$ such that the angles increments of (44) are extremely narrow. This allows us to replace the cosine in (47) by its first order Taylor expansion,

[2]This equation is only valid for $i \in [0, 90°[$. However this does not lead to any loss in generality as the problem is symmetric: for a negative inclination, a change of RAAN in the other direction will lead to the same intersection displacement.

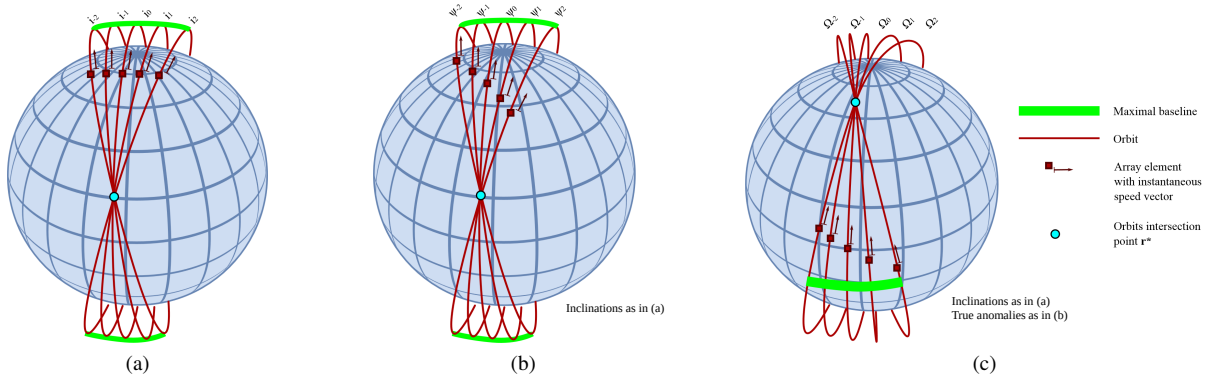

(a) (b) (c)

Fig. 9: Schematic representation of the array configurations varying: (a) only the orbital inclinations i_n ($\psi_n = 0$ and $\Omega_n = 0$). (b) both i_n and ψ_n. (c) i_n, ψ_n and Ω_n.

$\cos i_n \approx \pi/2 - i_n$, which leads to a precession rate that is proportional to n. A numerical example is carried out in sec. V-C.

The apsidal precession rate denoted as $\Delta\omega_n$ is equal to:

$$\Delta\omega_n = \frac{3\pi J_2 R_\oplus^2}{(R_\oplus + h)^2(1-e_n^2)^2}\left(2 - \frac{5}{2}\sin^2 i_n\right) \quad \text{rad/orbit.} \tag{48}$$

Due to $d_{act} \ll h + R_\oplus$, the sine function can likewise be expanded as a Taylor series in the inclinations: $\sin^2 i_n \approx 1-(i_n-\pi/2)^2$. Due to (44), the difference between the apsidal precession experienced by two difference array elements will thus be proportional to $[d_{act}/(h+R_\oplus)]^2$, which is vanishingly small. As a result, all elements of the array will experience the same apsidal precession, which does not endanger the flying formation. This is illustrated in the numerical application presented in sec. V-C.

The magnitude of air-drag and solar radiation pressure perturbations has not been evaluated since this would require an estimate of the physical cross-section of the satellites, which is outside the scope of this paper. However, we do not expect this is more critical than it is for existing LEO smallsats such as PROBA-V [23].

V. Experimental Results and Comparison with Single Configuration Radar Sounder

In this section, the performance models developed in the previous sections are applied to a practical acquisition scenario in order to understand the effectiveness of the proposed distributed radar sounder.

In Section V-A we describe the test scenario, while Section V-B addresses the distributed sounder system sizing and performance. A comparison with the performance of a single radar sounder is also performed. In Sections V-C and V-D, we discuss the orbital configuration and the expected performance degradation due to inaccuracy in the positioning of the sensors respectively.

A. Test Scenario

We consider an Earth observation scenario targeting icy (*e.g.*, Greenland and Antarctica) regions. We also consider as a possible additional test case Earth's arid regions (*e.g.*, Arabian Peninsula) within the same orbital configuration designed for the main test case. Two single configuration spaceborne VHF monostatic radar sounders named Orbiting Arid Subsurface and Ice Sheet Sounder (OASIS) and Satellite Radar Sounder for Earth Subsurface Sensing (STRATUS) [9] respectively have already been proposed for the aforementioned scenario [8], [7]. Accordingly, we consider the relevant radar parameters listed in Table I for designing the distributed radar sounder system and compare its performance to the single sounding configuration. In the distributed case we consider that each sensor deploys an omnidirectional radiator while for the single sounder we assume either a Yagi or a dipole antenna.

In [7], [8], the deployment of a 10 meter Yagi antenna is envisioned but no information is given about the gain or across-track beamwidth. Therefore we assume that the single sounder configuration used for comparison deploys a 10 meters Yagi antenna with parameters reported in [24]. The Yagi antenna across-track beamdwidth at -3dB is 20° and the one-way nadir gain is 12 dBi. In the along-track direction the Yagi antenna pattern is omnidirectional.

TABLE I: Assumptions for the distributed array performance analysis.

Parameter	Value
Orbit Height h	500 km
Main Target Earth Region	Icy (*i.e.*, poles)
Additional Target Earth Region	Arid (*i.e.*, equator)
Central Frequency	45 MHz
Bandwidth B	10 MHz
Transmitted Power P_t	800 W
Maximum Penetration Depth z_p	4 km (icy), 1 km (arid)
Antenna Type (distributed configuration)	Omni directional
Antenna Type (single configuration)	Dipole or Yagi

B. Distributed Sounder System Sizing and Performance

In this section, the sizing and performance of the distributed sounder array as a function of the initial assumptions on radar parameters (see Table I) are derived.

The central frequency of 45 MHz results in a wavelength $\lambda = 6.66$ m. According to (6), the across-track antenna beamwidth θ_b of the array is constrained to:

$$\theta_b \geq 0.15^\circ \tag{49}$$

By assuming a dielectric constant $\epsilon_r = 3.1$, which is representative of ice and sand [17], the bound for the minimum value of the first grating lobe according to (8) is:

$$\theta_g \geq 9.56^\circ \tag{50}$$

It follows that the best achievable resolution in across-track is $R_{act} = 1.14$ km which results in a resolution improvement $IRF = 6.77$, with respect to the conventional pulse-limited diameter $D_{pl} = 7.75$ km. The SCR improvement C_g is equal to 72 dB. To achieve the above performance a number of sensors $N = 65$ is required [see ((9))]. From the technological point of view, this number of sensors is rather large to deploy in a real scenario. However, it is possible to trade performance as function of N by performing a parametric analysis versus θ_b and θ_g given the bounds of (49) and (50). The parametric analysis is shown in Fig. 10 (a) and (b) for the IRF and SCR improvement. Moreover, the parametric value of d_{act} only depends on θ_g (see Fig. 10 (c)) and the maximum value of d_{at} as function of θ_g can be computed according to (16).The maximum allowed value of d_{at} is more stringent according to the no ambiguity criterion rather than the coherence one (see Fig. 10 (d)), except for the case $N = 65$.

In this study, without a loss in generality, we compare two configurations as function of the parameters: (i) trade-off configuration ($N = 21$) and (ii) high performance configuration ($N = 65$). For both configurations, the value of the first grating lobe is $\theta_g = 13.44^\circ$, which corresponds to the surface point equal to $2z_p$ (see (8)). This represents a margin value to avoid the peak ambiguity being exactly on the surface point corresponding to deepest sounded range which is assumed equal to 4 Km. The selection of $\theta_g = 13.44^\circ$ results in $d_{act} = 28.67$ m (see Fig. 10 (c)) and $d_{at} = 28.87$ m for $N = 21$ and $d_{at} = 28.37$ m for $N = 65$ (see Fig. 10 (d)). It follows that the nominal rotation angle θ_p is about 45°. The performance for both configurations are summarized in Table II, where a comparison with a single sounder configuration is also performed.

It is clear that a distributed sounder provides a substantial advantage in performance with respect to a single sensor configuration in terms of SCR and across-track resolution. As stated in Section II-B, the SNR improvement of the proposed distributed configuration is equal to N^2 [see (24)] when spatially correlated external noise sources are considered. The improvement is due to an increase in the equivalent antenna gain.

In our case, a factor equal to N of the distributed sounder gain has been used to scale the power transmitted by each sensor such that the overall distributed power is equivalent to having a single configuration sounder transmitting 800 W (see Table I). From the technological point of view, if the scaled power is too demanding for each distributed platform, another feasible option (see Section II-B) is to have one central large transmitting element and all the other deployed elements only receiving. According to Table II, the increase of two-way antenna gain with respect to the single sounder configuration adopting a dipole translates into an enhancement of the penetration capability of the instrument depending on the subsurface attenuation rate. The magnitude of the improvement in two-way antenna gain is estimated in the range between 13 ($N = 21$) and 18 ($N = 65$) dBi with respect to a single configuration with a linear dipole. The choice of apportioning a gain factor equal to N to reduce the transmitted power by each sensor results in a gain comparable with the Yagi antenna. In any case, the SCR improvement of the distributed configuration with that of a Yagi antenna or a dipole antenna is similar being the -3dB across-track beamwidth of the Yagi equal to 20°. This value is comparable to the maximum angular region for which subsurface returns are expected, therefore the Yagi antenna provides marginal clutter suppression (see Fig.11).

C. Orbit Configuration

As stated in Section V-A, we assume an Earth observation scenario where polar icy regions are the targets under investigation with the additional objective of sounding arid region at the equator. Accordingly, the distributed radar sounding system should form a full equivalent antenna length L_{act} over the poles (*i.e.*, latitude $\pm 90^\circ$) and the equator (*i.e.*, latitude 0°) under the assumption of a polar orbit at $h = 500$ km. This corresponds to an orbital period of 5668.31 seconds. Accordingly, we design the orbit to have the crossing point at latitude $r^*_\phi = 45^\circ$ [see (46)] and to overshoot the maximal baseline, which will be formed over latitude of $\pm 45^\circ$.

In order to have an across-track separation d_{act} of 28.67 m (see Table II) over both regions, the inclination of the sensors i_n, expressed in degrees, is equal to (44):

$$i_n = 90^\circ + n \arctan[d_{act}/(R_\oplus + h)] = 90^\circ + n0.000239^\circ \tag{51}$$

The RAAN Ω_n of each sensor, expressed in degrees, can be obtain by computing $g(i_n, r^* = 45^\circ)$:

$$\Omega_n = n \arctan[d_{act}/(R_\oplus + h)] = n0.000239^\circ \tag{52}$$

The true anomaly ψ_n of each sensor is computed by taking into account the along-track spacing d_{at} equal to 28.67 m, which acts as safety distance when the sensors pass-by the orbital nodes:

$$\psi_n = n \arctan[d_{at}/(R_\oplus + h)] = n0.000241^\circ \tag{53}$$

These results are summarised in Table II.

The nodal precession rate (see (47)) is equal to $\Delta\Omega_n = n3.66 \cdot 10^{-8}$ rad/orbit. The nodal precession has the effect of gradually: (i) shifting the crossing point from 45° to higher latitudes and (ii) increasing the across-track distance d_{act} between the sensors (see Fig. 12). Fig 13 reports the values of the rotation angle θ_p, grating angle θ_g, equivalent across-track antenna length $L_{act} = (N-1)d_{act}$ and beamwidth θ_b for 200 orbits versus latitude assuming the trade-off configuration ($N = 21$). According to performance metrics of Fig. 13, the

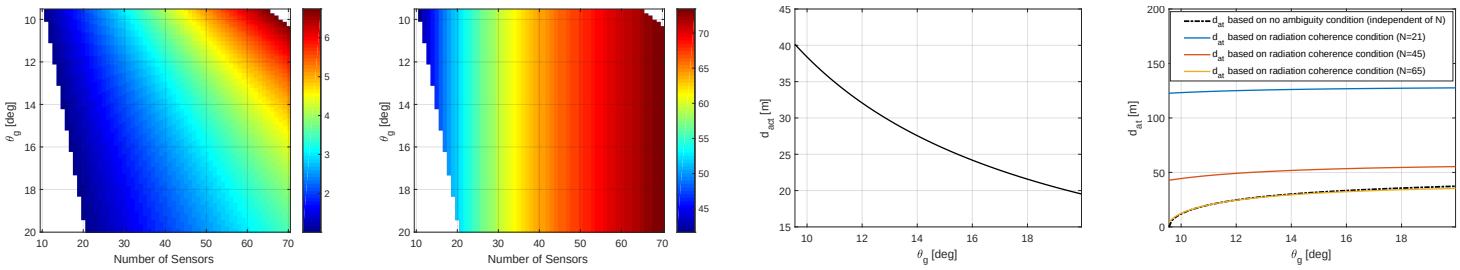

(a) (b) (c) (d)

Fig. 10: Parametric analysis as a function of θ_g and N for (a) Resolution improvement factor IRF (b) Clutter Improvement Factor C_g, (c) mutual distance between sensors d_{act}, and (d) along track spacing d_{at}. The region depicted in white in (a) and (b) represents parameter values where there is no performance improvement with respect to a single sounder configuration.

TABLE II: Distributed Radar Sounder Performance Summary(*).

PARAMETERS	DISTRIBUTED SOUNDER		SINGLE CONFIGURATION [7], [8]
	Trade-off Configuration	Very High Performance Configuration	
Number of sensors N	21	65	1
Orbit height h	500 km	500 km	500 km
Nominal across-track sensor distance d_{act}	28.67 m	28.67 m	-
Nominal along-track sensor distance d_{at}	28.87 m	28.37 m	-
Nominal Across-track beamwidth (-3dB) θ_b	$0.55°$	$0.17°$	$20°$ [Yagi] $64°$ [Dipole]
Nominal grating lobe θ_g	$13.44°$	$13.44°$	-
SCR Improvement C_g	52 dB	72 dB	-
Resolution Improvement Factor IRF	1.5	4.83	-
Two-way Antenna Gain	17.5 dBi	22.5 dBi	24 dBi [Yagi] 4.30 dBi [dipole]
Transmitted Power P_t	38 W (per sensor)	0.58 W (per sensor)	800 W (overall)
Orbit Inclination of the sensors i_n	$90° + n0.000239°$	$90° + n0.000239°$	-
RAAN of the sensors Ω_n	$n0.000239°$	$n0.000239°$	-
True anomalies of the sensors ψ_n	$n0.000241°$	$n0.000241°$	-
Nodal precession rate $\Delta\Omega_n$	$n3.66 \cdot 10^{-8}$ rad/orbit	$n3.66 \cdot 10^{-8}$ rad/orbit	-

(*)In the distributed case a gain factor equal to N_t of the total N_t^2 gain with respect to the single configuration has been used to reduce the transmitted power by each sensor. Therefore, for this particular case, the two-way antenna gain should be interpreted as $N_t G_0$ for the distributed case.

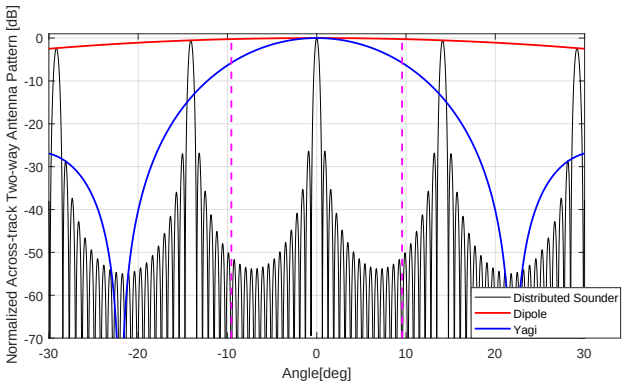

Fig. 11: Comparison of the Normalized Across-track radiation intensity for (a) Distributed Sounder, Trade-off configuration (Table II), (b) Single configuration (dipole antenna) and (c) Single configuration with Yagi antenna (see Table II). The lines in magenta mark the maximum angular span for which subsurface returns are expected (see (50).

array behaves as designed when deployed. As expected, the array rotates around its central element by a angle θ_p (see Fig. 9). Notable cases are the acquisition points (i.e. poles and equator) where $\theta_p = 45°$ as per construction for the first orbit and $\theta_p = 90°$ at the crossing point which implies that the sensors are all aligned and separated on the along-track direction only. At the poles the distributed sounder exhibits stable and nominal performance (see Table II) irrespective of the orbit. This is due to the fact that the modification of the right ascension, which is the only driver of the across-track separation at that particular point, does not change the inclination at the poles. As expected, at the crossing points no across-track baseline is formed thus leaving θ_b and θ_g undefined ($d_{act} \approx 0$). At the equator, the equivalent across-track antenna length increases with the number of orbits due to the nodal precession. This has the effect of reducing both θ_g and θ_b. Therefore, at the equator the nodal precession has the effect of increasing the distributed sounder performance in terms of clutter suppression and resolution while the first grating peak corresponds to lower clutter depths (see (8)). Since the maximum penetration depth for desert areas is $z_p = 1$ km (see Table I), the array can operate without orbit corrections for about 200 orbits, period after which the value of θ_g results in a grating peak positioned at 1 km equivalent

clutter depth (i.e. $\theta_g = 4.8°$).

For the main targets (*i.e.*, icy regions) nodal precession has no significant effect on performance. In the case that the additional test case (*i.e.*, arid regions) would be pursued, we believe that station-keeping is not to a critical issue with respect to nodal precession. The array elements can either be periodically repositioned every 200 orbits (13.12 days), or continuously corrected. Due to the fact that also the perturbation has some positive effects, namely the displacement of the crossing point (which allows greater global coverage) and the spreading of the array at the equator (which increases resolution), there is some merit to the idea of leaving the perturbation uncorrected for a limited period of time. Finally, the apsidal precession in (48) is identical for all satellite within 21 decimals, and stands at $\Delta\omega \approx 0.00438$ rad/orbit.

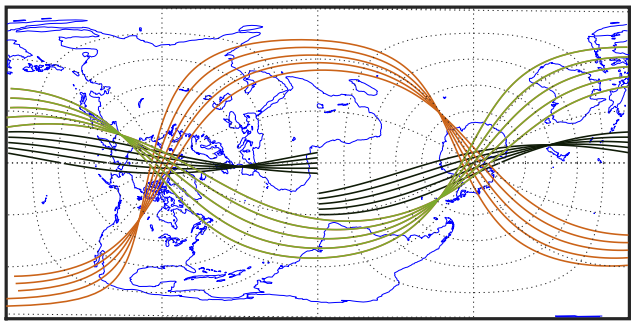

Fig. 12: Distributed radar sounder ground track for about one orbital period on the first orbit (black), the 50th orbit (red) and the 100th orbit (green). The nodal precession has the effect of increasing the latitude of the crossing points and the separation between sensors in across-track (not at the poles). For visualisation purposes, i_n and Ω_n are exaggerated and only five sensors are shown.

D. Evaluation of Performance Degradation due to Sensors Position Perturbation

In this section we evaluate the impact of potential sensors perturbations on the overall distributed radar sounder performance by considering the metrics in Section III (b).

As in Section III, we assume that the value of the peak power loss $P_{L,\text{nadir}}$ (42) is only impacted by sensor heights (z-direction) perturbations. Accordingly, to have significant degradations in the x and y directions, the unwanted displacement should be in the order of 200λ. In our test case this results in a value of unwanted displacement of 1.3 Km which is indeed a very large value. Fig. 14 shows the two-way peak power losses as function of the uncertainty standard deviation σ_z for a varying number of sensors. According to the results, a value of $\sigma_z = \lambda/10$ corresponding to 66 cm results in about 3 dB two-way losses, while a value of $\sigma_z = \lambda/4$ corresponds to 15 dB losses. The maximum peak power loss (*i.e.*, plateau of Fig.14) can be evaluated from (42) and is equal to N^2.

The peak-to-background losses (see (43)) exhibit a substantial variation with respect to the sensor positions uncertainty on all the three Cartesian axes and are also strongly dependent on the number of sensors. This behavior is shown in Fig. 15 where the isosurfaces for different values of $P_{L,\text{bg}}(\hat{\theta} = \theta_g/2)$ are shown. From the results of Fig. 15 the following considerations can be made. When small peak-to-background degradations are required, perturbations have to be kept small in all directions. If larger peak-to-background degradations are acceptable, then the limiting factor is σ_z only. In general, as the number of deployed sensors N increases, peak-to-background degradation becomes more sensitive to positioning errors. This is reported in Fig. 16 for the z-direction. To make an example, in order to have a degradation of 10 dB of the peak-to-background ratio for $N = 21$ then the standard deviation of the position uncertainty should not exceed $\sigma_x \leq \lambda/10$, $\sigma_y \leq \lambda/10$ and $\sigma_z \leq \lambda/20$. For $N = 65$ the values are much smaller and equal to $\sigma_x \leq \lambda/20$, $\sigma_y \leq \lambda/20$ and $\sigma_z \leq \lambda/40$.

As a final consideration, in the test scenario the synthesized across-track antenna pattern (see Fig. 11) has a nominal peak-to-background ratio of about 52 dB. As stated in Section III (b), the peak-to-background ratio impacts the clutter suppression capabilities of the system. Therefore larger degradation of it can be tolerated with respect to the peak power losses that instead impacts the subsurface penetration of the system. In radar sounding, the amount of subsurface penetration is a very important quantity with respect to the system performance.

In the next section we provide a discussion on several factors (*e.g.*, technological) affecting the distributed radar performance which should be taken into account when designing this type of systems.

VI. Discussion

A relevant challenge for the proposed distributed radar sounder system is the capability of maintaining coherence between satellites. A relevant result of our analyses is that the probing wavelength and the number of deployed sensors play a critical role in the robustness of the system. In particular height position accuracy (i.e. knowledge error) in the range $\lambda/10$ to $\lambda/20$ is required to have no degradation of the performance. Moreover, the required accuracy is to a great degree dependent on the number of deployed sensors N. It is important to state that the overall system performance increases with the number of deployed sensors, therefore the peak power losses due to height position accuracy are in part compensated by the increase in SNR. However, the peak to background losses, being a pure relative metric, are not compensated and they mostly affect the detectability of subsurface features. Here, we deal with HF/VHF sensors having wavelengths in vacuum ranging from 3 meters (*i.e.*, 100 MHz central frequency) up to 300 meters (1 MHz central frequency). Therefore in the worst case an accuracy of about 15 to 30 cm is required. This value is well within the modern inter-satellite links ranging accuracy in LEO orbit [25], [26], [27] . Note that the the sensor array could form a cooperative wireless network [16] such that it estimates the relative sensor positions and corrects for clocks drifts simultaneously.

In this study, we assumed that each sensor acts as an omnidirectional radiator. A dipole antenna is a very close approximation of this assumption. Examples of miniaturized dipole antenna architectures that can be used in our case are provided in [28], [29], [30]. The radiated power by radar

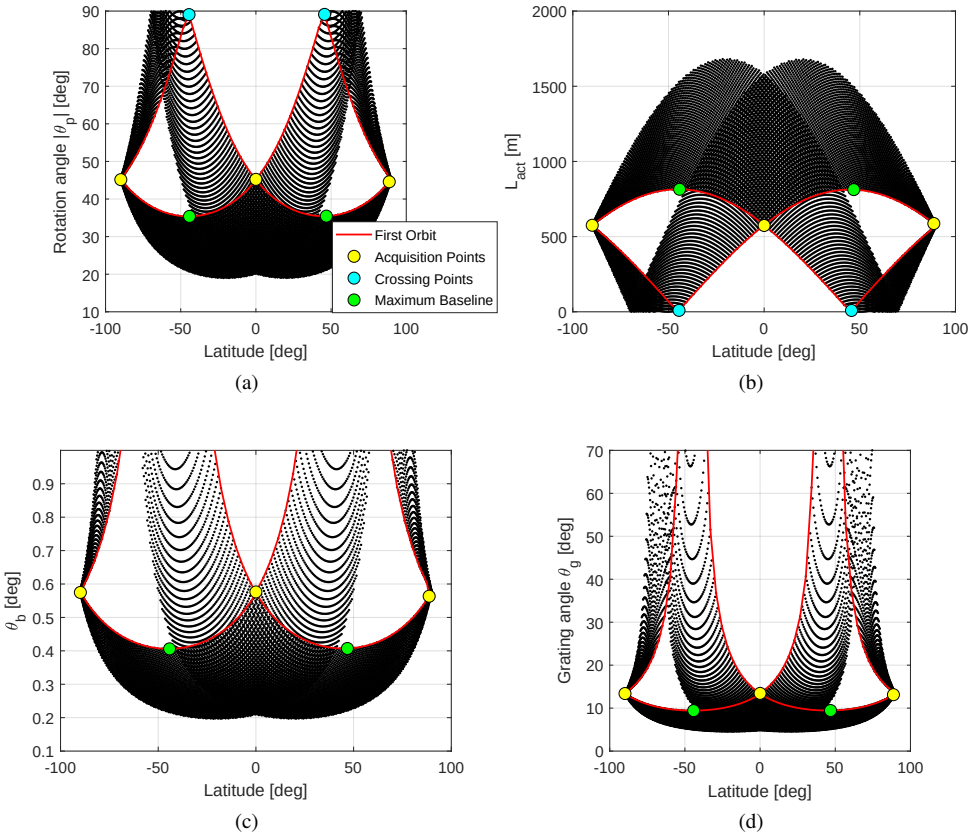

Fig. 13: Plot of (a) Rotation angle θ_p (absolute value), (b) Equivalent across-track antenna length L_{act}, (c) Across-track equivalent antenna beam-width θ_b and (d) First ambiguity angle θ_g versus latitude for 200 orbits assuming the trade-off configuration ($N = 21$). The acquisition points correspond to poles (icy regions) and the equator (arid regions). The red line indicates the performance values for the first orbit.

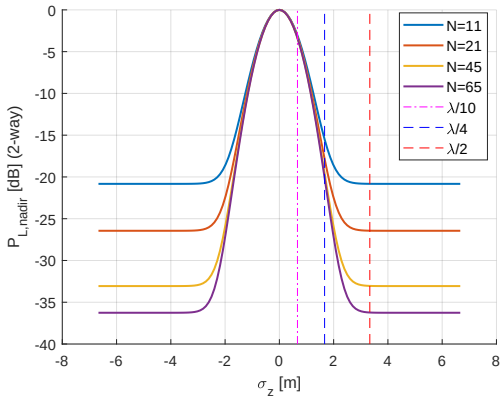

Fig. 14: Two-way peak power losses $P^2_{L,\text{nadir}}$ as function of σ_z for different number of sensors. Dashed lines corresponds to the equivalent normalisation σ_z/λ.

sounders are in the order of 10 W [2], [3] and never exceeding 800 W [8], [31]. As described in Section II-A, it is possible to trade the SNR gain of the distributed sounder with respect to a single sounder configuration to reduce the overall power transmitted by each sensor therefore circumventing technological limitations regarding the maximum radiated power. Under this assumption, each sensor requires a radiated power in the order of few Watts which is within reach of current technological development [32].

VII. Conclusion

Spaceborne radar sounders are valuable sensors operating in HF/VHF band for subsurface investigation of celestial bodies. The operating frequency is such that for mechanical reasons the deployed antenna generally illuminates large surface areas. This technological limitation considerably impacts the radar sounder performance resulting in very poor across-track resolutions and thus large off-nadir clutter which hinders the data interpretation.

In this paper, we proposed a novel distributed radar sounding concept and provided the mathematical model to predict its performance in terms of: (i) Distributed radar parameters, (ii) Orbital configuration, and (iii) Uncertainties in the positioning of the sensors. The performance predicted as function of the uncertainty in the position of the sensors should be interpreted as average quantities.

From the orbital point of view, we demonstrated that it is possible to find feasible and flexible orbit configurations meeting a given application need (*e.g.*, target regions) by adjusting the Keplerian parameters according to the equations developed in Section IV.

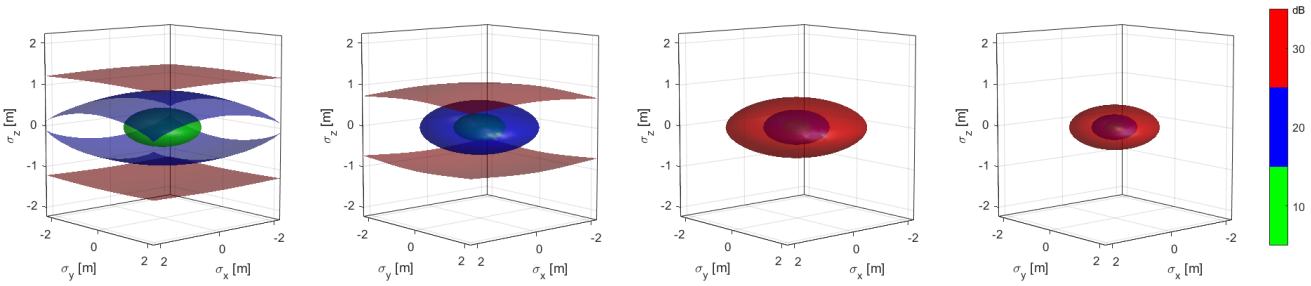

(a) (b) (c) (d)

Fig. 15: Isosurfaces of the two-way peak-to-background ratio $P^2_{L,\text{bg}}$ losses for (a) $N = 11$, (b) $N = 21$, (c) $N = 45$ and (d) $N = 65$ as function of σ_x, σ_y and σ_z evaluated at $\hat{\theta} = \theta_g/2$.

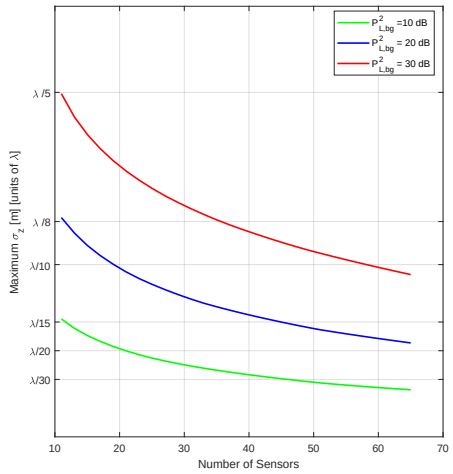

Fig. 16: Sensor position uncertainty σ_z (in units of λ) versus the number of sensors N for different values of peak to background ratio losses $P^2_{L,\text{bg}}$. The plot assumes σ_x and σ_y equal to 0.

While the distributed radar sounder modeling proposed in this work applies to any type of planetary bodies, to evaluate the performance of the proposed distributed radar sounder system we considered a meaningful Earth observation scenario targeting Earth's icy regions (*i.e.*, poles). We also assessed whether the same orbit configuration, devised for the main targets acquisition, could also be exploited for acquiring subsurface data over Earth's arid equatorial regions. The results show that orbital perturbations do not significantly affect the devised configuration. On the one hand, we observed an invariance in the distributed sounder performance as a function of the orbits at the poles. On the other hand, station-keeping operations are required after a number of orbits to compensate for nodal precession if arid region sounding wants to be paired with the icy region ones.

The results showed that the distributed sounding solution is particularly effective as it: (i) Reduces the impact of surface clutter, (ii) Increases the across-track resolution and (iii) increases the signal to noise ratio by a factor equal to the second power (worst case) or third power (best case) of the number of deployed sensors (or, alternatively, decreases the overall transmitted power with respect to a traditional radar sounder) with respect to a single sensor configuration. The gain factor value depends on the amount of correlation of the external noise source for the different receivers.

The sensor perturbations analysis showed that the required position accuracy is highly dependent on the number of sensors and becomes more stringent as the number of sensors increases. It is important to note that the proposed theoretical formulation for perturbation analysis represents average quantities and any specific orbit will be a random realization of these. As a general rule, a sensor height positioning accuracy between $\lambda/10$ and $\lambda/20$ is required for optimal performance. Being radar sounders operated in the HF/VHF band, this translates to required position accuracies on the order of half a meter. We provided evidence that this is within reach of current technological developments. Thus, in perspective, distributed radar sounding could be an interesting application for testing new radar formation flying technologies with respect to more challenging frequency bands (*e.g.*, C and X) where millimeter accuracies are required.

As future work, we plan to refine the design of the array by including more advanced array design techniques (e.g., use of overlapped subarrays), devise novel signal processing strategies which take advantage of the distributed architecture (*e.g.*, interferometric techniques) to retrieve geophysical parameters, and optimize the choice of orbits. Indeed we acknowledge that there could be other viable sensor deployment strategy, than the proposed one based on array tilting, which we plan to investigate. In any case, the proposed deployment strategy has the benefit of being the simplest, which allowed us to thoroughly treat it in this proof-of-concept paper.

ACKNOWLEDGMENT

The authors gratefully acknowledge D. Calabrese, S. Federici, M. Marabucci and L. Nardecchia of Thales Alenia Space Italy in Rome for their valuable suggestions and comments on the orbital part of this work. This work was supported by the Italian Space Agency (ASI) under the contract ASI n. 2016-14-U.O SaTellite Radar sounder for eArTh sUb-surface Sensing (STRATUS).

NOMENCLATURE

N	Number of sensors
d_{act}	Distance between sensors in the across-track direction
d_{at}	Distance between sensors in the along-track direction
d_p	Line of sight distance between sensors
L_{at}, L_{act}	Equivalent antenna length
λ	Radar wavelength
h	Sensor height
R_{act}, R_{at}	Resolution
θ_b	Across-track equivalent antenna beam-width
θ_g	First grating lobe (i.e. peak ambiguity angle)
ϵ_r	Subsurface dielectric constant (real part)
z_p	Maximum penetration depth
θ_p	Array rotation angle
D_{pl}	Pulse-limited diameter
B	Radar Bandwidth
c_0	Light speed in vacuum
IRF	Across-track resolution improvement factor
N_t	Total number of transmitting sensors
N_r	Total number of receiving sensors
N_{at}	Along-track gain and equivalent number of sensors
P_t	Transmitted power
G_0	Sensor antenna gain
σ	Radar cross section
P_r	Received Power
v_s	Sensor orbital velocity
PRI	Pulse Repetition Interval
P_n	Noise power
T	Equivalent receiver temperature
G_r	Range compression gain
T_s	Pulse Width
SNR	Signal to Noise Ratio
d	Euclidean distance between sensors and the ground
U	Two-way radiation intensity
$\hat{U}$	Normalized one-way radiation intensity
C_g	Clutter improvement factor
δ	Penetration depth
θ	Off-nadir angle
$\sigma_x, \sigma_y, \sigma_z$	Sensors position uncertainty standard deviations
$P_{L,\text{nadir}}$	One-way peak power losses
$P_{L,\text{bg}}$	One-way peak-to-background ratio losses
i	Inclination of the sensor
ψ	True anomaly of the sensor
Ω	RAAN
e	Eccentricity of the sensor
ω	Argument of the perigee of the sensor
r^*	Colatitude of the intersection point
$\Delta\Omega$	Nodal precession rate
$\Delta\omega$	Apsidal precession rate

APPENDIX A
DERIVATION OF THE RADAR EQUATION FOR THE DISTRIBUTED RADAR SOUNDER SYSTEM

We assume $i = 1, 2, ..N_t$ transmitting elements and $u = 1, 2, ..., N_r$ receivers for each along-track position $m = -(N_{at}-1)/2, ..., (N_{at}-1)/2$. For a nadir pointing radar, the surface scattered field denoted as E^s with respect to receive element u and transmit element i, and along-track position m is equal to [33]:

$$E^s_{uim} = \sqrt{\frac{2\eta P_{t_i} G_{0_i} \sigma_{ui} A_{e_u}}{(4\pi)^2 d^2_{im} d^2_{um}}} e^{jk(d_{im}+d_{um})} \tag{54}$$

where η is the intrinsic impedance of free space, P_{t_i} the time-averaged power transmitted by the ith element, G_{0_i} the antenna gain of the i-th element, σ_{ui} the bistatic radar cross section where u is the short notation for the incident angle and i the one of the scattering angle, A_{e_u} is the antenna aperture for the u-th receiving element, k is the wave number, d_{im} and d_{um} are the radial distance from the target to the i-th transmitter and u-th receiver at the m-th along-track position. We assume that the flying formation is such that electromagnetic waves coherence is maintained for every u, i, m. This is equivalent to state that:

$$-\lambda/4 \leqslant d_{im} - h \leqslant \lambda/4 \tag{55}$$

$$-\lambda/4 \leqslant d_{um} - h \leqslant \lambda/4 \tag{56}$$

where h is the sensors height. In radar sounding, h is consistently larger than the relative distance between sensors, thus we can assume monostatic scattering and $d_{im} = d_{um} \approx h$. This also implies that the incident angle and scattering angle are very similar and thus we can assume $\sigma_{ui} = \sigma$. We assume that all the transmit/receive elements are identical and thus $G_{0_i} = G_0$, $A_{e_u} = A_e = \frac{G_0 \lambda^2}{4\pi}$ and $P_{t_i} = P_t$. According to the above analysis, the expression of E^s_{uim} of (54) is equal to:

$$E^s_{uim} = \sqrt{\frac{2\eta P_t G_0 \sigma A_e}{(4\pi)^2 h^4}} e^{j2kh} \tag{57}$$

The total electric field amplitude E_t recollected for a given target is equal to:

$$E_t = \sum_{m}^{N_{at}} \sum_{u}^{N_r} \sum_{i}^{N_t} E^s_{uim} \tag{58}$$

and the total received power P_r is equal to:

$$P_r = \frac{E_t E_t^*}{2\eta} = \frac{N_t^2 N_r^2 N_{at}^2 P_t G_0^2 \sigma \lambda^2}{(4\pi)^3 h^4} \tag{59}$$

APPENDIX B
DERIVATION OF THE AVERAGE PERTURBED ELECTRIC FIELD AND ONE-WAY RADIATION PATTERN

In this Appendix, the derivation of (36) is presented. The demonstration is done in detail for a reduced case with z-direction perturbations only, which can be straightforwardly generalized to the case of three-dimensional perturbations. The surface electric field of a linear array is obtained through (28) setting $N_{at} = 1$:

$$\Psi(x, y) = \sum_n \frac{A_n}{d_n(x, y)} e^{jkd_n(x,y)} \equiv \sum_n \psi_n(x, y), \tag{60}$$

where the index n upon which the sum is carried out is given by

$$n = -\frac{N-1}{2}, ..., \frac{N-1}{2} \tag{61}$$

The one-dimensional derivation strongly resembles that given in [34], [35], where unidimensional displacements on the surface of a parabolic antenna are treated.

A. Reduced case of z-perturbations only

Under the perturbation $z_n \to z_n + \delta^z_n = h + \delta^z_n$, where δ^z_n is a random quantity, the perturbed distance $\tilde{d}_n$ evolves as:

$$\tilde{d}_n(x, y) = \sqrt{(x - x_n)^2 + y^2 + (h + \delta^z_n)^2}. \tag{62}$$

Assuming $\delta^z_n \ll h$, we can perform a Taylor series in δ^z_n for $d_n(x, y)$ and $d_n(x, y)^{-1}$, as both appear in $\psi_n(x, y)$. We

obtain $\tilde{d}_n(x,y) = d + hd^{-1}\delta_z + \mathcal{O}(\delta_z^2)$ for the distance and $\tilde{d}_n(x,y)^{-1} = d^{-1} - hd^{-3}\delta_z + \mathcal{O}(\delta_z^2)$ for the inverse distance [some (x,y) and n dependences have been dropped for clarity].

Inserting those expression in $\psi_n(x,y)$, the perturbed waveform $\tilde{\psi}_n(x,y)$ can be expressed as follows:

$$\tilde{\psi}_n(x,y) \approx \psi_n(x,y)\left(1 - \frac{h\delta_z}{d^2}\right)e^{ik\frac{h\delta_z}{d}}, \tag{63}$$

The expectation value of this expression over the perturbation δ_n^z, $\langle\psi_n(x,y)\rangle_{\delta_z}$ can be computed if δ_n^z obeys a particular distribution. Assuming a zero-mean Gaussian distribution of standard deviation σ, $\delta_n^z \sim \mathcal{N}(0,\sigma)$, and using the property that, for a random variable X described by a probability density function $f_X(\xi)$, the expected value of a function $g(X)$ of that random variable is given by $\langle g(X)\rangle = \int_{-\infty}^{+\infty} g(\xi)f_X(\xi)d\xi$, we have

$$\left\langle\tilde{\psi}_n(x,y)\right\rangle_{\delta_z} = e^{-\frac{1}{2}\left(\frac{hk}{d}\right)^2\sigma^2}\left(1 - i\frac{kh^2}{d^3}\sigma^2\right)\psi_n(x,y) \tag{64}$$

The second term of the amplitude factor is of order $\mathcal{O}(k\sigma^2/d)$, which makes it negligible with respect to the term 1. This can be understood physically: this factor comes from the perturbation of the $1/d$ factor in the initial field, which is responsible for spherical spreading losses. The full expression of the ensemble-averaged perturbed field, assuming a zero-mean Gaussian perturbation on the z-components of the position of the array elements, is therefore given by

$$\left\langle\tilde{\Psi}(x,y)\right\rangle_{\delta_z} \approx \sum_n e^{-\frac{1}{2}\left(\frac{hk}{d_n(x,y)}\right)^2\sigma^2}\frac{1}{d_n(x,y)}e^{ikd_n(x,y)} \tag{65}$$

The expectation value of the perturbed two-way radiation pattern $\langle\tilde{U}\rangle_{\delta_z} = \langle\tilde{\Psi}\tilde{\Psi}^\dagger\rangle_{\delta_z}$ is slightly more complex to compute. Factoring the deterministic elements out of the ensemble-average operator, we have

$$\left\langle\tilde{U}(x,y)\right\rangle_{\delta_z} = \sum_n\sum_{n'}\psi_n\psi_{n'}^\dagger\left\langle e^{ikh\left(\frac{\delta_n^z}{d_n} - \frac{\delta_{n'}^z}{d_{n'}}\right)}\right\rangle. \tag{66}$$

If $n = m$, the expression inside the exponential cancels, so that $\langle e^{(\cdots)_{nn'}}\rangle = 1$. On the other hand, if $n \neq m$, by applying the same reasoning as above, we find $\langle e^{(\cdots)_{nn'}}\rangle = e^{-\frac{1}{2}h^2k^2\left[\left(\frac{\sigma_n}{d_n}\right)^2 + \left(\frac{\sigma_{n'}}{d_{n'}}\right)^2\right]}$. Thus, assuming naturally $\sigma_n = \sigma_{n'} \equiv \sigma$, the expectation value of the perturbed power can be written as

$$P = \sum_n |\psi_n|^2 + \sum_n\sum_{n'}\left[I - \delta_{nn'}\right]\psi_n\psi_{n'}^\dagger e^{-\frac{1}{2}h^2k^2\sigma^2\left(\frac{1}{d_n^2} + \frac{1}{d_{n'}^2}\right)}, \tag{67}$$

where $I = \mathbf{1}_{N\times N}$ is the identity tensor and $\delta_{nn'}$ Kronecker's delta.

B. Generalisation to three-dimensional perturbations

Generalising (66) and (67) to three-dimensional perturbations is straightforward. Under the perturbations (34), the distance between a spacecraft element n and a point (x,y) on the surface evolves as:

$$\begin{aligned} d_n(x,y) \to \tilde{d}_n(x,y) = \Big\{ & \left[x - (x_n + \delta_n^x)\right]^2 \\ & + \left[y - (y_n + \delta_n^y)\right]^2 \\ & + \left[h + \delta_n^z\right]^2 \Big\}^{\frac{1}{2}} \end{aligned} \tag{68}$$

Considering that the perturbations are much smaller than the distances between array elements and points on the ground, *i.e.*, $\delta_n^x \ll x - x_n$ (likewise on y-perturbations) and $\delta_n^z \ll h$, we may compute a multivariate Taylor series of the above expression:

$$\begin{aligned} \tilde{d}_n(x,y) = d_n(x,y) &+ \frac{x - x_n}{d_n(x,y)}\delta_n^x + \frac{y - y_n}{d_n(x,y)}\delta_n^y \\ &+ \frac{h}{d_n(x,y)}\delta_n^z + \mathcal{O}(\delta_n^x, \delta_n^y, \delta_n^z)^2 \end{aligned} \tag{69}$$

Inserting this expression into the field $\psi_n(x,y)$ of an array element, we obtain

$$\tilde{\psi}_n(x,y) \approx \psi_n(x,y)e^{ik\left(\frac{x-x_n}{d_n(x,y)}\delta_n^x + \frac{y-y_n}{d_n(x,y)}\delta_y + \frac{h}{d_n(x,y)}\delta_n^z\right)} \tag{70}$$

Thanks to the separability of $\tilde{\psi}_n(x,y)$ itself, and to the fact that the probability distributions of δ_x, δ_y, and δ_z are independent from each other, the action of the ensemble-average operator is conveniently separable:

$$\begin{aligned} \left\langle\tilde{\psi}_n(x,y)\right\rangle_{\delta_x,\delta_y,\delta_z} = &\psi_n(x,y)\left\langle e^{ik\frac{x-x_n}{d_n(x,y)}\delta_n^x}\right\rangle_{\delta_x} \\ &\left\langle e^{ik\frac{y-y_n}{d_n(x,y)}\delta_n^y}\right\rangle_{\delta_y}\left\langle e^{ik\frac{h}{d_n(x,y)}\delta_n^z}\right\rangle_{\delta_z}. \end{aligned} \tag{71}$$

From that expression, a reasoning very similar to the one-dimensional case leads naturally to (36).

REFERENCES

[1] L. J. Porcello, R. L. Jordan, J. S. Zelenka, G. F. Adams, R. J. Phillips, W. E. Brown, S. H. Ward, and P. L. Jackson, "The apollo lunar sounder radar system," *Proceedings of the IEEE*, vol. 62, no. 6, pp. 769–783, June 1974.

[2] R. Croci, R. Seu, E. Flamini, and E. Russo, "The shallow radar (sharad) onboard the nasa mro mission," *Proceedings of the IEEE*, vol. 99, no. 5, pp. 794–807, May 2011.

[3] L. Bruzzone, G. Alberti, C. Catallo, A. Ferro, W. Kofman, and R. Orosei, "Subsurface radar sounding of the jovian moon ganymede," *Proceedings of the IEEE*, vol. 99, no. 5, pp. 837–857, May 2011.

[4] L. Carrer, C. Gerekos, and L. Bruzzone, "A multi-frequency radar sounder for lava tubes detection on the moon: Design, performance assessment and simulations," *Planetary and Space Science*, vol. 152, pp. 1–17, 2018.

[5] R. Thomas, E. Frederick, J. Li, W. Krabill, S. Manizade, J. Paden, J. Sonntag, R. Swift, and J. Yungel, "Accelerating ice loss from the fastest greenland and antarctic glaciers," *Geophysical Research Letters*, vol. 38, no. 10, 2011.

[6] A. Shepherd, E. R. Ivins, A. Geruo, V. R. Barletta, M. J. Bentley, S. Bettadpur, K. H. Briggs, D. H. Bromwich, R. Forsberg, N. Galin *et al.*, "A reconciled estimate of ice-sheet mass balance," *Science*, vol. 338, no. 6111, pp. 1183–1189, 2012.

[7] A. Freeman, X. Pi, and E. Heggy, "Radar sounding through the earths ionosphere at 45 mhz," *IEEE Transactions on Geoscience and Remote Sensing*, vol. 55, no. 10, pp. 5833–5842, 2017.

[8] E. Heggy, P. A. Rosen, R. Beatty, T. Freeman, and Y. Gim, "Orbiting arid subsurface and ice sheet sounder (oasis): Exploring desert aquifers and polar ice sheets and their role in current and paleo-climate evolution," in *Geoscience and Remote Sensing Symposium (IGARSS), 2013 IEEE International*. IEEE, 2013, pp. 3483–3486.

[9] L. Bruzzone *et al.*, "Stratus satellite radar sounder for earth subsurface sensing (cee10/001)," *answer to Call for Earth Explorer-10 Mission Ideas, ESA/EXPLORER/EE-10*, 2017.

[10] S. El Maghraby, A. Kiyoshi, A. Grubisic, C. Colombo, and A. Tatnall, "A novel interferometric microwave radiometer concept using satellite formation flight for geostationary atmospheric sounding," *IEEE Transactions on Geoscience and Remote Sensing*, 2018.

[11] G. Krieger, I. Hajnsek, K. P. Papathanassiou, M. Younis, and A. Moreira, "Interferometric synthetic aperture radar (sar) missions employing formation flying," *Proceedings of the IEEE*, vol. 98, no. 5, pp. 816–843, 2010.

[12] S. Bandyopadhyay, G. P. Subramanian, R. Foust, D. Morgan, S.-J. Chung, and F. Hadaegh, "A review of impending small satellite formation flying missions," in *53rd AIAA Aerospace Sciences Meeting*, 2015, p. 1623.

[13] G. Galati and G. Losquadro, "Distributed-array radar system comprising an array of interconnected elementary satellites," Jun. 27 1989, uS Patent 4,843,397. [Online]. Available: https://www.google.com/patents/US4843397

[14] G. Fasano, M. DErrico, G. Alberti, S. Cesare, and G. Sechi, "P-band distributed sar," in *Distributed Space Missions for Earth System Monitoring*. Springer, 2013, pp. 527–545.

[15] A. J. Boonstra, M. Garrett, G. Kruithof, M. Wise, A. van Ardenne, J. Yan, J. Wu, J. Zheng, E. K. A. Gill, J. Guo, M. Bentum, J. N. Girard, X. Hong, T. An, H. Falcke, M. Klein-Wolt, S. Wu, W. Chen, L. Koopmans, H. Rothkaehl, X. Chen, M. Huang, L. Chen, L. Gurvits, P. Zarka, B. Cecconi, and H. de Haan, "Discovering the sky at the longest wavelengths (dsl)," in *2016 IEEE Aerospace Conference*, March 2016, pp. 1–20.

[16] R. T. Rajan, A.-J. Boonstra, M. Bentum, M. Klein-Wolt, F. Belien, M. Arts, N. Saks, and A.-J. van der Veen, "Space-based aperture array for ultra-long wavelength radio astronomy," *Experimental Astronomy*, vol. 41, no. 1-2, pp. 271–306, 2016.

[17] F. T. Ulaby, R. K. Moore, and A. K. Fung, "Microwave remote sensing active and passive," 2015.

[18] R. J. Mailloux, *Phased array antenna handbook*. Artech House Boston, 2005, vol. 2.

[19] R. Heimiller, J. Belyea, and P. Tomlinson, "Distributed array radar," *IEEE Transactions on Aerospace and Electronic Systems*, no. 6, pp. 831–839, 1983.

[20] J. E. Harvey, D. Bogunovic, and A. Krywonos, "Aberrations of diffracted wave fields: distortion," *Applied optics*, vol. 42, no. 7, pp. 1167–1174, 2003.

[21] G. O. Reynolds *et al.*, *The New Physical Optics Notebook: Tutorials in Fourier Optics*. ERIC, 1989.

[22] P. Fortescue, G. Swinerd, and J. Stark, *Spacecraft systems engineering*. John Wiley & Sons, 2011.

[23] G. Huby, R. P. Kleihorst, K. Mellab, and L. Grignard, "Proba-v, a vegetation satellite," in *Sensors, Systems, and Next-Generation Satellites XIV*, vol. 7826. International Society for Optics and Photonics, 2010, p. 78260R.

[24] D. Blankenship, B. Edwards, Y. Kim, P. Geissler, D. Gurnett, W. Johnson, W. Kofman, J. Moore, D. Morse, R. Pappalardo *et al.*, "Feasibility study and design concept for an orbiting ice-penetrating radar sounder to characterize the three-dimensional distribution of subsurface water on europa," Technical Report, Jet Propulsion Laboratory, California Institute of Technology, Tech. Rep., 1999.

[25] Y. Yang, Y. Li, C. Rizos, A. G. Dempster, and X. Yue, "Inter-satellite ranging augmented gps relative navigation for satellite formation flying," *The Journal of Navigation*, vol. 67, no. 3, pp. 437–449, 2014.

[26] S. D'Amico, J.-S. Ardaens, and S. De Florio, "Autonomous formation flying based on gpsprisma flight results," *Acta Astronautica*, vol. 82, no. 1, pp. 69–79, 2013.

[27] O. Montenbruck, M. Delpech, J.-S. Ardaens, N. Delong, S. DAmico, and J. Harr, "Cross-validation of gps-and ffrf-based relative navigation for the prisma mission," in *4th ESA workshop on satellite navigation user equipment technologies. NAVITEC*. Citeseer, 2008.

[28] S. Gao, Y. Rahmat-Samii, R. E. Hodges, and X.-X. Yang, "Advanced antennas for small satellites," *Proceedings of the IEEE*, vol. 106, no. 3, pp. 391–403, 2018.

[29] Y. Rahmat-Samii, V. Manohar, and J. M. Kovitz, "For satellites, think small, dream big: A review of recent antenna developments for cubesats." *IEEE Antennas and Propagation Magazine*, vol. 59, no. 2, pp. 22–30, 2017.

[30] J. Oh, J. Choi, F. T. Dagefu, and K. Sarabandi, "Extremely small two-element monopole antenna for hf band applications," *IEEE Transactions on Antennas and Propagation*, vol. 61, no. 6, pp. 2991–2999, 2013.

[31] T. Ono and H. Oya, "Lunar radar sounder (lrs) experiment on-board the selene spacecraft," *Earth, planets and space*, vol. 52, no. 9, pp. 629–637, 2000.

[32] E. Peral, E. Im, L. Wye, S. Lee, S. Tanelli, Y. Rahmat-Samii, S. Horst, J. Hoffman, S.-H. Yun, T. Imken *et al.*, "Radar technologies for earth remote sensing from cubesat platforms," *Proceedings of the IEEE*, vol. 106, no. 3, pp. 404–418, 2018.

[33] D. Jenn, Y. Loke, T. C. Hong Matthew, Y. E. Choon, O. C. Siang, and Y. S. Yam, "Distributed phased arrays and wireless beamforming networks," *International Journal of Distributed Sensor Networks*, vol. 5, no. 4, pp. 283–302, 2009.

[34] P. Rocca, N. Anselmi, A. Massa, T. Moriyama, and D. Bresciani, "Interval-based tolerance analysis with localized surface errors in parabolic reflectors," in *Antenna Measurements & Applications (CAMA), 2014 IEEE Conference on*. IEEE, 2014, pp. 1–3.

[35] S. Sinton and Y. Rahmat-Samii, "Random surface error effects on offset cylindrical reflector antennas," *IEEE transactions on antennas and propagation*, vol. 51, no. 6, pp. 1331–1337, 2003.